

# Spectral matching based on discrete particle swarm optimization: A new method for terrestrial water body extraction using multi-temporal Landsat 8 images

Kai Jia<sup>a,b</sup>, Weiguo Jiang<sup>a,b,\*</sup>, Jing Li<sup>a,b</sup>, Zhenghong Tang<sup>c</sup>

<sup>a</sup> Key Laboratory of Environmental Change and Natural Disaster of Ministry of Education, Faculty of Geographical Science, Beijing Normal University, Beijing 100875, China

<sup>b</sup> Beijing Key Laboratory for Remote Sensing of Environment and Digital Cities, Faculty of Geographical Science, Beijing Normal University, Beijing 100875, China

<sup>c</sup> Community and Regional Planning Program, College of Architecture, University of Nebraska-Lincoln, Lincoln, NE 68588-0105, USA

## ARTICLE INFO

### Keywords:

Discrete particle swarm optimization (DPSO)  
Flood inundation mapping  
Landsat 8 Operational Land Imager (OLI)  
Surface water extraction

## ABSTRACT

Terrestrial water, an important indicator of inland hydrological status, is sensitive to land use cover change, natural disaster and climate change. An accurate and robust water extraction method can determine the surface water distribution. In this paper, a new method, called the spectrum matching based on discrete particle swarm optimization (SMDPSO) is proposed to recognize water and nonwater in Landsat 8 Operational Land Imager (OLI) images. Only two parameters, the standard water spectrum and the tile size, are considered. These parameters are sufficiently stable so it is unnecessary to change their values for different conditions. By contrast, in supervised methods, samples are chosen based on conditions. Eight test sites covering various water types in different climate conditions are used to assess the performance relative to that of unsupervised and supervised methods in terms of overall accuracy (OA), kappa coefficients (KC), commission error (CE) and omission error (OE). The results show that: (1) SMDPSO achieves the highest accuracy and robustness; (2) SMDPSO has lower OE but higher CE than the supervised method, which means that SMDPSO is the least likely to misclassify water as nonwater, but is more likely to misclassify nonwater as water; (3) SMDPSO has advantages with respect to removing shallows and dark vegetation and preserving the real distribution of small ponds, but cannot recognize shadows, ice, or clouds without the help of other data such as DEM. In addition, a case of flooding in north-eastern China is analyzed to demonstrate the applicability of SMDPSO in water inundation mapping. The findings of this study demonstrate a novel robust, low-cost water extraction method that satisfies the requirements of terrestrial water inundation mapping and management.

## 1. Introduction

Terrestrial water bodies such as rivers, lakes, ponds, puddles and artificial reservoirs play important roles in inland water cycles and ecosystem balance and provide essential resources for animals and vegetation. Although terrestrial water bodies cover a small proportion of the Earth's surface area (2–3%, Raymond et al., 2013), they are estimated to account for 10% of animals and 35% of vertebrates (Stendera et al., 2012) and are therefore significant for biological diversity and ecosystem functions. However, inland water is undergoing a loss of biological diversity worldwide, which is endangering the futures of these ecosystems (Dudgeon et al., 2006). Changes in surface water may lead to disasters such as floods, landslides, debris flows and water shortages, which may result in substantial economic cost and loss of

life. The social, economic and ecological responses to surface water inundation have been studied in recent literature (Marton and Kapelan, 2014; Tang et al., 2016; Ten Brinke et al., 2017; Zhang et al., 2017), providing guidance for government officials and decision-makers in policy and management.

Advances in remote sensing technology enable large-scale terrestrial water monitoring. Landsat satellites (Landsat 4, 5, 7, and 8) have seven bands, from the visible spectrum to infrared, at 30-m spatial resolution, including a coarse-resolution thermal band. The historical inventory includes time series from the 1980s to the present, which satisfy the requirements of high spatial resolution and long-term continuous monitoring. Moderate Resolution Imaging Spectroradiometer (MODIS) images include 36 bands at 250-m spatial resolution, and the ability to conduct observation every day at the same site enables near real-time

\* Corresponding author at: Key Laboratory of Environmental Change and Natural Disaster of Ministry of Education, Faculty of Geographical Science, Beijing Normal University, Beijing 100875, China.

E-mail addresses: [jiakai@mail.bnu.edu.cn](mailto:jiakai@mail.bnu.edu.cn) (K. Jia), [jiangweiguo@bnu.edu.cn](mailto:jiangweiguo@bnu.edu.cn) (W. Jiang).

<https://doi.org/10.1016/j.rse.2018.02.012>

Received 18 April 2017; Received in revised form 2 February 2018; Accepted 9 February 2018

Available online 23 February 2018

0034-4257/ © 2018 Elsevier Inc. All rights reserved.

monitoring at a large scale. Based on the detailed information contained in remote sensing satellite images, researchers can recognize surface water and map its spatial distribution to analyze the relationships among water and other factors. Water classification methods are detailed in the references (Feyisa et al., 2014). Here, three types of methods are summarized: (1) the water index for water spectral characteristics; (2) conventional land cover classification; and (3) water-specific classification methods such as expert systems.

The simplest method is the water index. McFeeters (1996) first proposed the normalized difference water index (NDWI) to identify water using bands 2 (green) and 4 (NIR) of Landsat TM. Rogers and Kearney (2004) replaced bands 2 and 4 with bands 3 (red) and 5 (MIR) of Landsat TM to compute the NDWI to reduce signature variability in unmixed coastal marshes. Because of the influence of built-up land, vegetation and soil, Xu (2006) used bands 2 (green) and 5 (MIR) of Landsat TM to evaluate the modified NDWI (MNDWI), which is one of the most commonly used water indices. Subsequently, Feyisa et al. (2014) found that previously proposed water indices are constrained by low accuracy in various situations. Therefore, they introduced the automated water extraction index (AWEI), which uses more bands (bands 2, 4, 5 and 7 of Landsat TM) to achieve greater robustness and remove shadows in mountainous areas. Because of the imperfection of any single water index, researchers have also combined multiple indices to improve accuracy (Yamazaki et al., 2015). The water index method is popular because its calculations are simple and its results appropriate. However, higher accuracy is sometimes required, which makes more complex classification methods appealing. Machine learning for supervised classification is a reasonable way to save time and labor while maintaining satisfactorily high accuracy. Mueller et al. (2016) used 180,000 samples to train eCognition to separate 26 classes, which provided substantial prior knowledge for computer learning. These samples were input into a regression tree model to classify water across Australia. Supervised classification methods have been developed for all possible land types, not just water. Water indices and supervised classification can be implemented jointly to improve the specific training of supervised classification for water. For example, Tulbure et al. (2016) computed water indices (e.g., NDWI, AWEI and normalized difference moisture index) and vegetation indices (e.g., enhanced vegetation index) as explanatory variables to highlight water information, which was then processed with a random forest model. However, this combination doesn't take full use of the water-specific information in classifiers. Therefore, a water-specific classification method was developed. Yang et al. (2015) applied a fuzzy clustering method to account for spatial information in water extraction from heterogeneous backgrounds. Pekel et al. (2016) used an expert system for high-resolution mapping of global surface water. This water-specific classifier achieves higher accuracy than that of general supervised methods.

Heuristic optimization algorithms, such as particle swarm optimization (PSO), have been introduced into remote sensing to recognize water-specific information. PSO was first proposed by Kennedy & Eberhart et al. (1995) and has since been modified by several researchers, the most common version of which was proposed by Shi and Eberhart (1998). The combination of PSO and the classification algorithm proved to be useful. For example, PSO has been combined with support vector machine (SVM) to obtain physical parameters such as chlorophyll concentrations in offshore waters (Bazi and Melgani, 2007), indicating that PSO overcame the insufficiency of training samples. PSO was also applied to hyper-spectral imagery processing to reduce the redundant dimensionality. Yang et al. (2012) used PSO for supervised optimal band searching and the selective result was taken as the input of SVM to classify urban land cover. To take advantage of heuristic algorithms, PSO and genetic algorithm were integrated with SVM to dramatically increase the classification accuracy and effectively recognize roads in an urban background (Bhatt et al., 2014). Discrete particle swarm optimization (DPSO) has recently been used for sub-pixel classification. DPSO resolved problems in discrete space and was

utilized by Li et al. (2015a, 2015b, 2016) to map sub-pixel-scale flood inundation.

Deficiencies are present in the studies summarized above: (1) previous water index methods consider only a few bands with information loss for other bands. For example, the NDWI used only two out of six bands, and the AWEI used four of six bands. (2) The sample collection step required by supervised classification is time consuming, and prior human knowledge greatly influences the accuracy. Therefore, supervised classification may not be stable at a large scale. (3) Water specific classification achieves greater accuracy, but still encounters the problem of sampling. Furthermore, few studies have been conducted for the water-specific classifier. This paper continues the research (Yang et al., 2015; Pekel et al., 2016) on water-specific classification and proposes a new water extraction method called spectrum matching based on discrete particle swarm optimization (SMDPSO). Compared with the water index method, SMDPSO incorporates a new water information mining method to fully utilize all the band information and simultaneously suppress nonwater noise. An advantage over the supervised method is that SMDPSO requires no samples, fewer parameters and no manual intervention. DPSO is introduced into the water classification process to strengthen water-specific information with water classifier.

The objectives of this paper are (1) to propose a novel water extraction method (SMDPSO); (2) to assess the accuracy and sensitivity of SMDPSO in either test sites; (3) to present a case study of flood inundation mapping for a flood in northeastern China by means of SMDPSO.

## 2. Test sites and materials

Eight test sites from around the world, which feature different climates, water types and landscapes, were chosen to examine the robustness and general applicability of SMDPSO. In addition, Northeast China was selected as a case study of inundation mapping for the practical application of SMDPSO. Landsat 8 OLI images were used as the only data source to avoid the influence of different sensors. Pre-processing was also conducted.

### 2.1. Test sites and case study area

The eight test sites (Fig. 1 and Table 1) include (A) thermokarst lakes in Tuktoyaktuk, Canada; (B) the Amazon River in Manaus, Brazil; (C) Hamburg, Germany; (D) the Yobe River Valley, Nigeria, in dry (D1) and wet (D2) season; (E) the coastal plains of the Bay of Bengal; (F) the lower reaches of the Yellow River in Kaifeng, China; and (G) Coongie Lakes National Park, Australia. The water bodies of Canada and Australia consist of lakes, representing puddles and periglacial lakes in a subarctic climate and saline lakes in a hot desert climate, respectively. The Yobe River Valley has clear wet and dry seasons, with a hot semi-arid climate. Therefore, two tests were conducted, one for the dry season and another for the wet season, to evaluate the seasonal sensitivity of the method. Manaus is located at the confluence of the Rio Negro and Solimoes River, which are influenced by a tropical rainforest climate. The Rio Negro is called the Black River because its water resembles strong tea, which is attributed to its humic acid content. The Solimoes River appears yellow because a substantial proportion of clays and sands from the mountains are suspended in the water. The Bay of Bengal is characterized by a tropical monsoon climate with a dense water network. Hamburg, Germany and Kaifeng, China were selected because urban waters are also important in the study of urban flood disasters; these cities have a temperate oceanic climate and a cold semi-arid climate, respectively. Hamburg is famous as an aquatic city with numerous canals. In the areas around Kaifeng, a vast number of ponds and are crossed by the Yellow River, whose water is yellow because of its high suspended sand content. The selected sites are located in areas with flat topography to avoid the influence of terrain shadows (Table 1).



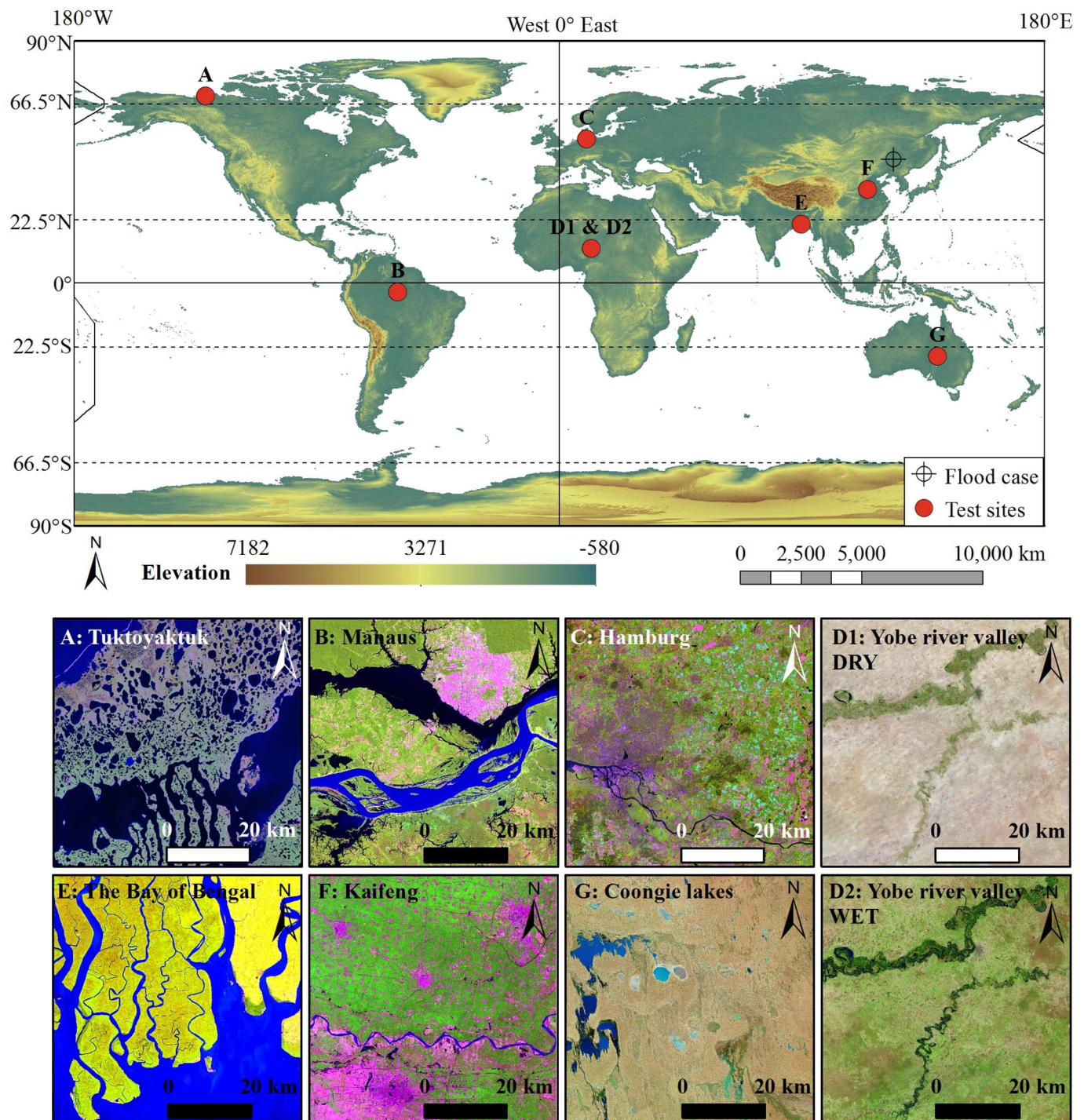


**Fig. 1.** Location of the eight test sites and flooding example case. The flooding case is a flood that occurred in northeastern China in 2013. A) Thermokast lakes in Tuktoyaktuk, Canada, 09/Jul/2013. B) The confluence of two different waters in Manaus, Brazil, 27/Jul/2016. C) Urban water in Hamburg, Germany, 12/May/2016. D1) Dry season water in the Yobe River valley, Nigeria, 23/Feb/2016. D2) Wet season water in the Yobe River Valley, Nigeria, 18/Sep/2016. E) Dense water systems in the Bay of Bengal, 12/Nov/2015. F) Ponds and sandy water in Kaifeng, China, 04/May/2016. G) Coongie Lakes, Australia, 06/Nov/2016. Images of A–G subplots are all from Landsat 8 OLI sensor in false color composite of SWIR 1, NIR and green bands. (For interpretation of the references to color in this figure legend, the reader is referred to the web version of this article.)

Northeastern China was selected for the practical application of the proposed method to a case study of inundation mapping (Fig. 1). This region experienced heavy flooding, which covered parts of both China and Russia, between August and September 2013. Considerable land area was inundated along the Heilongjiang, Songhuajiang and Nenjiang Rivers. In China, three provinces and 3.73 million people were affected, which resulted in the loss of 78 million RMB. The affected area in China extended from 45°N to 48°N latitude and 123°E to 124°E longitude.

Only a small portion of this area located at 46°N latitude and 124°E longitude is shown in herein (Fig. 1) to clearly present the details of the inundation.

## 2.2. Materials

The proposed method relies on sensors (i.e., Landsat 5, 7 and 8), but it does not study the sensitivity to sensors. Landsat 8 OLI images were

**Table 1**

Test sites characteristics and validation data sources which are all from Landsat 8 OLI. These images are clipped to  $2000 \times 2000$  pixels to allow reasonable assessment of the proposed method with higher water proportions. The longitude and latitude extents of test sites are shown in Table S1. Climate type is the Koeppen Climate System from FAO.

Code	Test sites (Country)	Characteristics	Climates (Koeppen key)	Landsat path/row	Date
A	Tuktoyaktuk (Canada)	Puddles/Thermokarst lakes/Shallow	Subarctic (Dfc)	062/11	09/Jul/2013
B	Manaus (Brazil)	High sand content/High humic acid concentration/High vegetation cover	Tropical rainforest (Af)	231/62	27/Jul/2016
C	Hamburg (German)	Urban water mixed with artificial buildings	Temperate oceanic (Cfb)	195/23	12/May/2016
D1	Yobe River valley (Nigeria)	Dry season/Low vegetation cover with less water	Hot semi-arid (Bsh)	186/51	23/Feb/2016
D2	Yobe River valley (Nigeria)	Wet season/Higher vegetation cover with more water	Hot semi-arid (Bsh)	186/51	18/Sep/2016
E	The Bay of Bengal (Bangladesh)	Dense water systems	Tropical monsoon (Am)	137/45	12/Nov/2015
F	Kaifeng (China)	High sand content/Ponds/Urban water mixed with artificial buildings	Cold semi-arid (Bsk)	123/36	04/May/2016
G	Coongie Lakes (Australia)	Saline/Less water	Hot desert (Bwh)	097/079	06/Nov/2016

the only data source used and were divided into two types, validation data and auxiliary data, for different goals.

The validation data (Table 1) from Landsat 8 OLI were downloaded from the Earth Resources Observation and Science Center (EROS) (USGS, 2017a). The OLI images contain nine bands: four visible bands, three infrared bands, one panchromatic band and one cirrus band. However, only the visible and infrared bands, a total of seven bands, were used in this study. One image is used for each test site, except for the two images used for the Yobe River Valley to represent the dry and wet seasons. All selected images are cloudless to decrease the influence of clouds on the data.

Auxiliary data are required for the evaluation and discussion to provide information about the influences of noise (Table 2) and different water types (Table 3) on classification. The sources of noises include clouds, cloud shadows on surface, hill shadows, snow and ice. Water types include deep inland lakes, shallow inland lakes, rivers and seawater. All the data listed in Tables 2 and 3 are from Landsat OLI images to maintain consistency with the validation data.

The case study of inundation mapping for flooding in northeastern China also requires images, which are from Landsat 8 OLI images with few clouds from 2013 to 2016, of which the path/row numbers are 119/28. Landsat 8 was launched in 2013; therefore, inundation mapping using Landsat 8 covers only 2013 and later. Because of the large number of images used (a total of 30 images), they are not listed in a table.

### 2.3. Data pre-processing

The raw downloaded Landsat images are represented by digital numbers (DN), with unitless and relative values. To make the pixel values comparable between images, they are transferred to the top of atmospheric reflectance via radiometric calibration (USGS, 2017b).

Landsat OLI provides a view across a 185-km swath, and very low

**Table 2**

Auxiliary dataset I: Landsat 8 OLI images showing the influence of shadows, snow/ice, and clouds.

Path/row	Date	Location	Factors
113/26	16/Aug/2015	Amur River, Russia's Far East	Cloud and shadow casted
151/34	07/Aug/2014	Wakhan Corridor, Afghanistan	Hill shadow and snow
062/11	26/Oct/2014	Tuktoyaktuk, Canada	Ice

**Table 3**

Auxiliary dataset II: Landsat 8 OLI images for selection of the standard water spectrum.

Path/row	Date	Location	Water type
172/65	30/Jul/2016	Tanganyika Lake, Africa	Inland deep lake
119/38	13/Oct/2015	Taihu Lake, China	Inland shallow lake
113/26	29/Aug/2014	Amur River, Russia's Far East	River water
096/43	21/Apr/2016	Pacific Ocean	Seawater

proportions of water are observed at this range, resulting in over-estimated water extraction accuracy. Therefore, all images were clipped to  $2000 \times 2000$  pixels (approximately 60 km) to achieve higher water percentages and lower visual interpretation costs.

The validation data were visually classified as water or nonwater to estimate the accuracy of this method. The spatial resolution of Landsat images (30 m) is too large to identify small patches with mixed pixels. Therefore, Google Earth and Bing Maps, which provides high-resolution overviews with historical images at times approximately consistent with Landsat passes were used as supplements for visual interpretation.

### 3. Methods

This section consists of three parts. First, the fundamentals of SMDPSO are introduced in detail. Second, the assessment methods, including the accuracy and sensitivity analysis, are presented. Third, a brief introduction of inundation mapping in Northeast China is provided.

#### 3.1. SMDPSO algorithm

SMDPSO was designed to extract water from multispectral images, such as those of the Landsat satellites series. Two steps are necessary (Fig. 2): (1) obtain the water probability images from multispectral data via the proposed spectral matching (SM) method; and (2) identify water pixels from the water probability images through the objective function resolved using DPSO. The advantage of this method is that it achieves high accuracy similar to supervised classification while maintaining the low costs of unsupervised methods, with fewer parameters, minimal prior knowledge and high automation potential.

##### 3.1.1. Obtaining water probability via spectral matching

Water reflectance is low and decreases monotonically from the visible to infrared bands. Additionally, an approximately standard spectrum of water can be obtained from typical water areas in some images. The water probability is defined as the difference between this



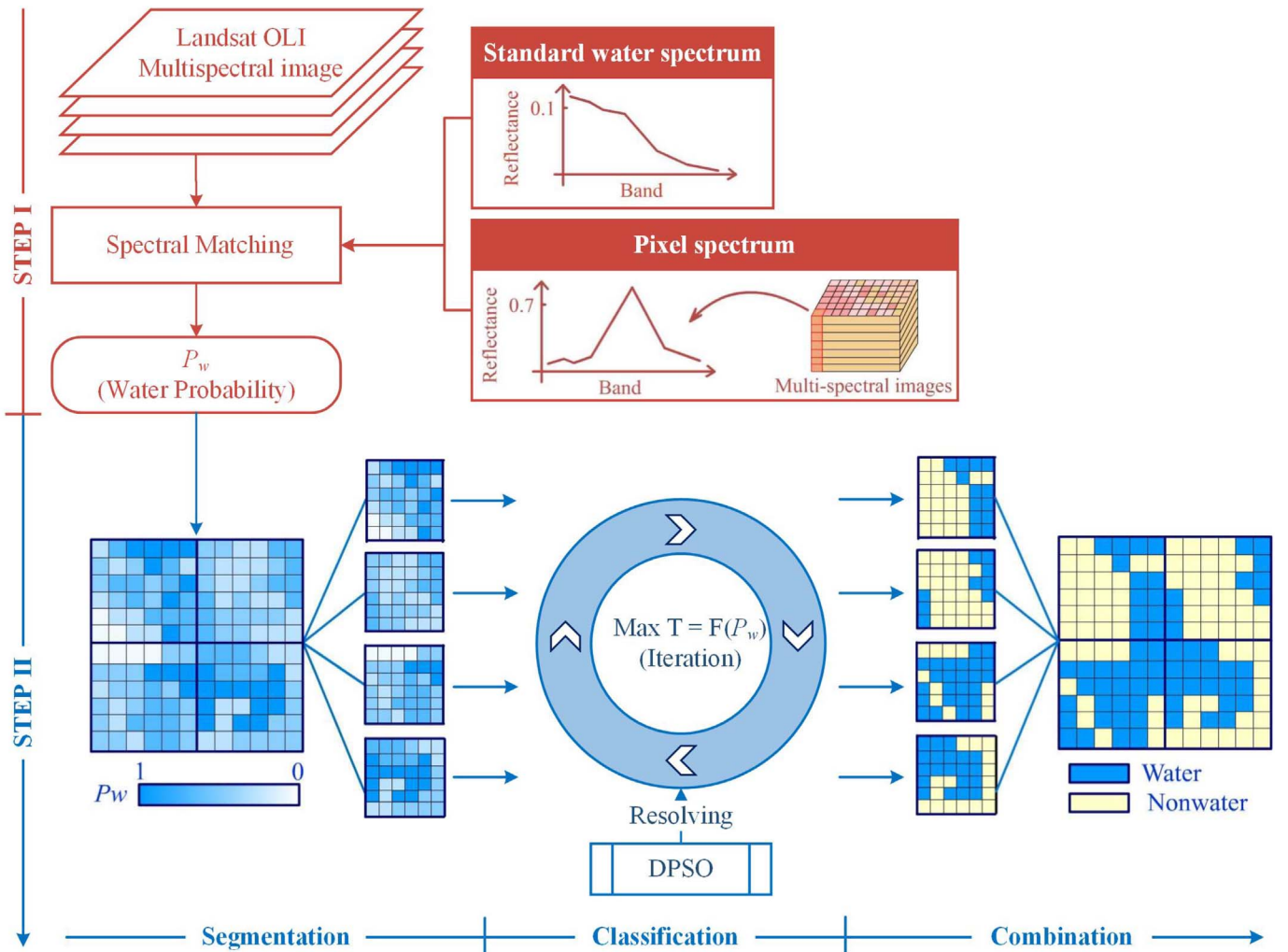


Fig. 2. Flow diagram of SMDPSO. The standard water spectrum was obtained from a Landsat 8 OLI image.  $F(P_w)$  is the function of  $P_w$ , which is objective function.

standard water spectral curve and the spectral curves of the targets. Greater differences in the spectra represent a lower water probability. In this paper, the standard water spectrum for Landsat 8 OLI images is  $\{0.1153, 0.0942, 0.0779, 0.0715, 0.0324, 0.0055, 0.0031\}$  (each value represents the TOA reflectance of a band). A discussion of standard water spectral selection is provided in Section 3.2.2.

The variables  $\vec{W} = (w_1, w_2, \dots, w_b)$  and  $\vec{O} = (o_1, o_2, \dots, o_b)$  represent the spectral vector (i.e., the spectral curve) of typical water and ground objects, respectively, and  $b$  is the number of bands. To reflect and exaggerate the relative differences between various bands, the vectors are normalized with min-max scaling.

The water probability (Eq. (1)) can be defined as the product of the cosine (Eq. (2)) and distance (Eq. (3)) similarities:

$$P_w = \cos(\vec{W}, \vec{O}) \cdot \text{dist}(\vec{W}, \vec{O}), \quad (1)$$

$$\cos(\vec{W}, \vec{O}) = \frac{\vec{W} \cdot \vec{O}}{\|\vec{W}\| \cdot \|\vec{O}\|}, \quad (2)$$

$$\text{dist}(\vec{W}, \vec{O}) = 1 - \frac{1}{\sqrt{b}} \sqrt{\sum_{i=1}^b (w_i - o_i)^2}. \quad (3)$$

The cosine similarity and distance similarity are values between 0 and 1. So the water probability is in the range [0, 1]. A higher value of  $P_w$  indicates greater probability of water.

The nonwater probability can then be defined by Eq. (4):

$$P_{nw} = 1 - P_w. \quad (4)$$

### 3.1.2. Constructing an objective function for water classification

The ground is a continuous surface, and the occurrence of water depends on the neighboring pixels. Images are divided into tiles with the size of  $rows \times cols$ . For example, if  $rows$  and  $cols$  are both set to 6, the class of each individual pixel in the area of  $6 \times 6$  pixels is determined relative to the other 35 pixels. A single image includes many such tiles. In Fig. 2, the image is divided into four tiles with  $rows$  and  $cols$  equal to 6. Each tile represents one classification process, where the pixel is classified as water or nonwater by maximizing the objective function (Eq. (5)) resolved by DPSO. This classification continues until  $T$  reaches the maximum value (Fig. 3), as follows:

$$\max T = c_1 \cdot \sum_{k=1}^{rows \times cols} P_{w,k} + c_2 \cdot \sum_{k=1}^{rows \times cols} P_{nw,k} - c_3 \cdot \frac{\bar{D}_{nearest}}{\sqrt{rows^2 + cols^2}}, \quad (5)$$

where  $c_1$ ,  $c_2$  and  $c_3$  are constants set according to Table 4, that represent the weight of the water portion, nonwater portion and neighborhood;  $P_w$  is the water probability when the pixel is water,  $P_{nw}$  is the nonwater probability when the pixel is nonwater; and  $\bar{D}_{nearest}$  is the nearest distance from one water pixel to another water pixel in the same tile (Eq. (6)).

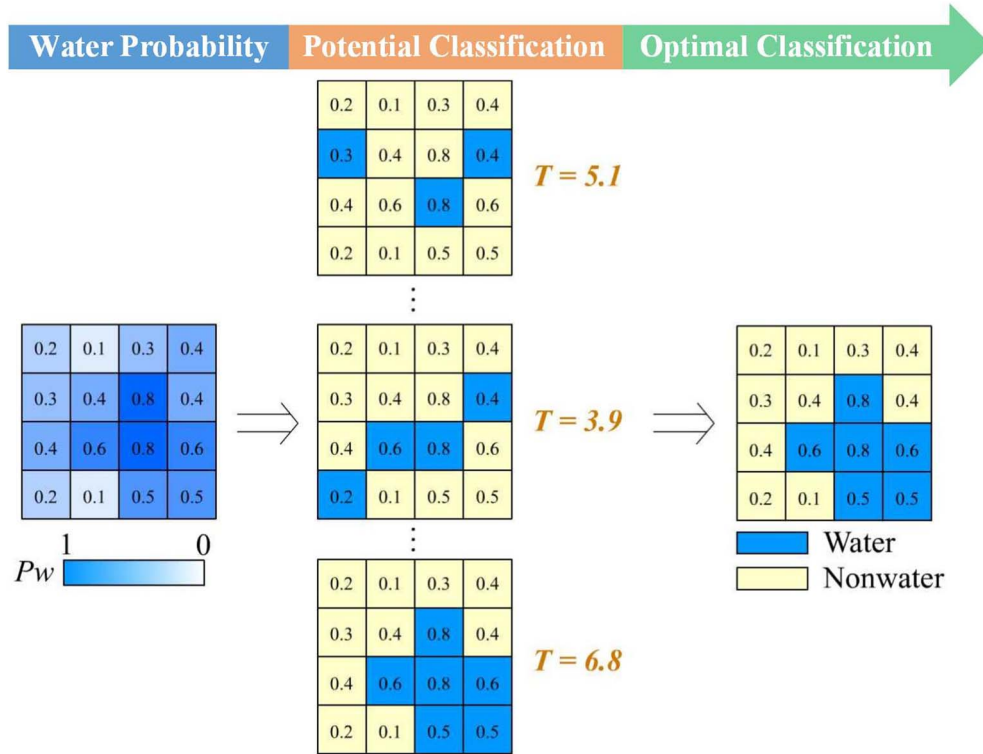


Fig. 3. An example of classification determined with objective function.  $P_w$  is the water probability. The best classification is the one with the maximal value of  $T$ .

Table 4

Values and meanings of  $c_1$ ,  $c_2$  and  $c_3$  in the objective function;  $\mu$  is the mean of pixels in a tile with a size of  $rows \times cols$ , and  $\sigma$  is the standard deviation for the same tile. Descriptions are the potential and ambiguous classes that are changing in each iteration of water classifier.

Mode	Condition	$c_1$	$c_2$	$c_3$	Description (dubious and ambiguous)
H	$\mu/\sigma > 20$	0.9	0.7	1	Homogeneous water or nonwater
M	$3 < \mu/\sigma \leq 20$	1	1	1	Heterogeneous nonwater
LL	$\mu/\sigma < 3$ and $\mu \leq 0.25$	2	0.5	1.5	Small tributaries
LH	$\mu/\sigma < 3$ and $\mu > 0.25$	0.9	0.5	1	At the junction of land and water

which reflects the ability of the method to recognize small water bodies, is divided into LL and LH depending on the mean values. A higher deviation indicates heterogeneity, which may reflect mixed pixels of small water areas and nonwater. When the mean is lower (Mode LL), small tributaries may be present. In this mode,  $c_1$  is much larger than  $c_2$  to differentiate small water bodies from vast land areas. In addition, the connectivity of tributaries is accounted for by increasing  $c_3$ . When the mean is higher (Mode LH), there may be a junction between land and water. In this mode,  $c_1$  is smaller, but still greater than  $c_2$ , because the amount of water is sufficient in the transition zones. All the values of  $c_1$ ,  $c_2$ ,  $c_3$  and the thresholds of  $\mu$ ,  $\sigma$  in Table 4 are identified through numerous experiments.

$\bar{D}_{nearest}$

$$= \begin{cases} 0, & \text{No water} \\ \sqrt{rows^2 + cols^2}, & \text{Number of water is equal to 1} \\ \text{Nearest distance from one pixel to another,} & \text{otherwise} \end{cases} \quad (6)$$

The weight of every part,  $c_1$ ,  $c_2$  and  $c_3$ , can be determined via different modes (Table 4) that can be viewed as the initialization before the first iteration of classifier. To make the classification more sensitive to various land surfaces, four modes (H, M, LL and LH) were implemented (Table 4) based on the means ( $\mu$ ) and standard deviations ( $\sigma$ ) of the pixels whose values are the water probabilities in  $rows \times cols$ . Mode H represents high-probability surfaces where the features are very likely to be either homogeneous water or nonwater, because the mean of the tile is greater, and the standard deviation is lower. In this mode, water is indicated by  $c_1$  greater than  $c_2$ . Mode M represents moderate probability, where mixed nonwater pixels occur, because the standard deviation is very large. The determination of which pixels are water and which are nonwater is challenging because of the interference of features similar to water; therefore,  $c_1$  is equal to  $c_2$ . Mode L,

### 3.1.3. Resolving the objective function using discrete particle swarm optimization

If the image is divided into  $n$  tiles, the resolving process is repeated  $n$  times. Therefore, only one tile is considered below. DPSO is an optimization algorithm that resolves problems in discrete space, and it was used by Li et al. (2015a, 2015b, 2016) to map sub-pixel-scale flood inundation.

Given a tile with size of  $D = rows \times cols$ , the feasible solution  $\{x_1, x_2, \dots, x_D\}$  is defined as Eq. (7):

$$x_d = \begin{cases} 0, & \text{if } d^{th} \text{ pixel is nonwater} \\ 1, & \text{if } d^{th} \text{ pixel is water} \end{cases} \quad (7)$$

DPSO considers every feasible solution as a particle with  $N$  dimensions. Each particle has location  $x$ , speed  $v$  and adaptation  $T$ ;  $x$  is defined in Eq. (7). Adaptation  $T$  is the  $T$  in the objective function (Eq. (5)). The speed  $v$  is defined as Eq. (8). Location  $x$  is updated in each iteration according to Eqs. (8)–(10):

$$v_{id}^{k+1} = wv_{id}^k + s_1r_1(p_{id} - x_{id}^k) + s_2r_2(p_{gd} - x_{id}^k), \quad (8)$$

$$v_{id}^{k+1} = \begin{cases} v_{max}, & \text{if } v_{id}^{k+1} > v_{max} \\ v_{id}^{k+1}, & \text{if } v_{min} \leq v_{id}^{k+1} \leq v_{max} \\ v_{min}, & \text{if } v_{id}^{k+1} < v_{min} \end{cases}, \quad (9)$$

$$x_{id}^{k+1} = \begin{cases} 1, & \text{if } L(v_{id}^k) > R \\ 0, & \text{otherwise} \end{cases}, \quad (10)$$

$$w = w_{max} - \frac{w_{max} - w_{min}}{k} \times k_{max}, \quad (11)$$

$$L(v_{id}^k) = \frac{1}{1 + e^{-v_{id}^k}}, \quad (12)$$

where  $i$  is the  $i$ th particle,  $d$  is the  $d$ th dimension,  $k$  is the  $k$ th iteration, and  $w$  is the inertia weight. In standard PSO,  $w$  is defined as Eq. (11);  $w_{max}$  and  $w_{min}$  are generally set to 0.95 and 0.4, respectively (Shi and Eberhart, 1998); and  $k_{max}$  is the maximum of the iterations. Constants  $s_1$  and  $s_2$  are accelerating factors, which are often both set to 2.05 (Kennedy and Eberhart, 1995).  $r_1$ ,  $r_2$  and  $R$  are random numbers distributed uniformly within  $[0, 1]$ .  $r_1$  and  $r_2$  are generated differently for each particle, whereas,  $R$  is generated once for each iteration. The variable  $p_{id}$  is the historically optimal solution for the  $i$ th particle, and  $p_{gd}$  is the globally optimal solution for all particles;  $v_{max}$  and  $v_{min}$  are the permissible maximum and minimum speeds, respectively. Without limitation, that is, a speed  $v$  outside the interval  $[0, 1]$ , a particle could escape from the feasible region. Therefore, the maximum and minimum are set to 1 and 0, respectively, for this study. Finally,  $L()$  is the (Eq. (12)).

DPSO is applied to each tile as follows (Fig. 4):

- (1). Randomly generate  $I$  particles with  $D$  dimensions, such as matrix  $X$  (Eq. (13)). Note that  $X$  is a 0–1 matrix. Randomly generate the corresponding speed matrix, such as  $V$ , where  $V$  is limited by Eq. (9).

$$X = \begin{bmatrix} x_{11}, x_{12}, \dots, x_{1D} \\ x_{21}, x_{22}, \dots, x_{2D} \\ \vdots \\ x_{I1}, x_{I2}, \dots, x_{ID} \end{bmatrix} \quad (13)$$

$$V = \begin{bmatrix} v_{11}, v_{12}, \dots, v_{1D} \\ v_{21}, v_{22}, \dots, v_{2D} \\ \vdots \\ v_{I1}, v_{I2}, \dots, v_{ID} \end{bmatrix} \quad (14)$$

- (2). For each line of  $X$ , the pixels in the tile are divided into two categories: water and nonwater. Calculate adaptation  $T$  for each line of  $X$  according to Eq. (5). The historically optimal values for each line are set to  $X$  because there are no historical values. The globally optimal values are set to the line that has the maximum value of adaptation  $T$  in the historically optimal values.
- (3). Compute new  $V$  using Eqs. (8) and (9). Update  $X$  using Eq. (10).
- (4). Calculate adaptation  $T$  for each line of  $X$ . Based on comparison of  $T$  in each line of  $X$  in this iteration and the previous iteration, the historically optimal values are set to the larger  $T$ .
- (5). If  $k$  is equal to  $k_{max}$ , proceed to (6); otherwise, return to (3).
- (6). The globally optimal values are the final classification for water and nonwater in this tile. Move to another tile and repeat the above steps.

### 3.2. Assessment methods

The assessment included two concepts: accuracy assessment to measure how close the SMDPSO classification results were to the real world and sensitivity analysis to determine the influence of some factors (i.e., input parameters and specific features) on the accuracy.

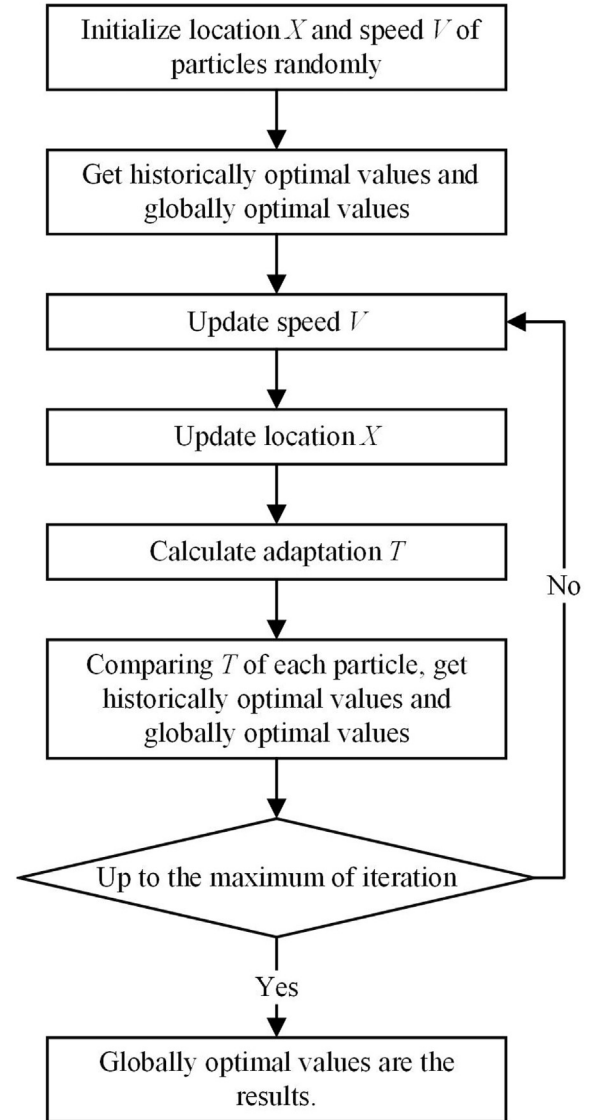


Fig. 4. Flow diagram of DPSO.

#### 3.2.1. Accuracy assessment methods

The confusion matrix method (Ron and Foster, 1998), by which the overall accuracy (OA), kappa coefficients (KC), commission error (CE) and omission error (OE) can be calculated, was applied to estimate the accuracy of SMDPSO. Two unsupervised methods, the iterative self-organizing data analysis techniques algorithm (IsoData) and K-Means, and three supervised methods, maximum likelihood (ML), neural network classification (NNC) and the support vector machine (SVM) method, were compared. For unsupervised methods, at least 10 classes were preset and were merged later into the same classes as the supervised methods. Training samples for the supervised methods were taken from different sites and included different classes in the corresponding conditions. See Table S2 for more details on training samples.

#### 3.2.2. Sensitivity analysis method

The sensitivity analysis was performed to assess how the (1) water spectrum, (2) tile size and (3) specific features influenced the classification accuracy. The water spectrum and tile size were the input parameters of SMDPSO.

SMDPSO was conducted relative to the standard water spectrum. Four sites (Tanganyika, Taihu, Amur and the Pacific, see Fig. 5) were selected to assess the sensitivity of SMDPSO to water type. Tanganyika



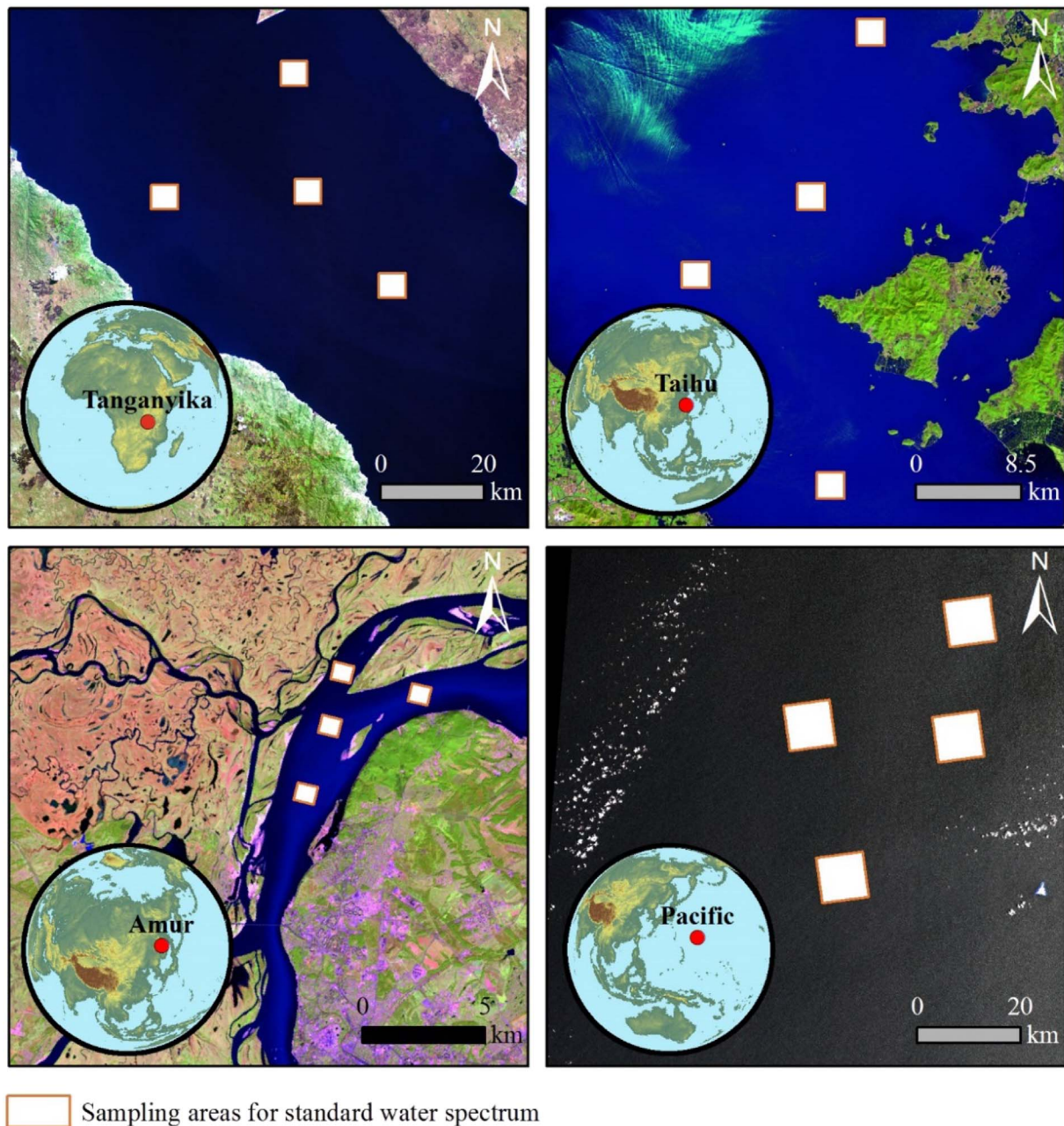


**Fig. 5.** Sampling areas of water spectra from different sites around the world. Tanganyika and Taihu are inland lakes, with deep and shallow water, respectively. Amur represents river water. The Pacific represents ocean water. The different water spectra sampled from these four sites are the means of points in each sampling area. Images are all from Landsat 8 OLI sensor in false color composite of SWIR 1, NIR and green bands. Date acquired: Tanganyika, 30/Jul/2016; Taihu, 13/Oct/2015; Amur, 29/Aug/2014; Pacific 21/Apr/2016. (For interpretation of the references to color in this figure legend, the reader is referred to the web version of this article.)

is a lake that is > 1000-m deep. Taihu is a shallow lake with a maximum depth of < 3 m. Amur is a river and the Pacific Ocean is an open water system without inland influence. The standard water spectrum used in SMDPSO, which was obtained from the Amur River.

Tile size is an important parameter for SMDPSO. Greater sizes covered more neighboring pixels but require more computing time due to the uncertainty. All eight test sites (A–G) were used to compute OA for tile sizes from 4 to 12.

### 3.3. Water inundation mapping method

The water inundation frequency can be determined based on water classification images, but it is not sufficient to reflect surface water distribution patterns on the ground. With time series data, the binary

classification is reclassified with three types and four subtypes to provide more information about the water environment (Fig. 6). The three types are nonwater, temporary water and permanent water, which are regrouped into four subtypes: seasonal melt land, seasonal inundation, permanent water and nonwater. Seasonal melt land is land that is covered by snow or ice in winter and/or spring but is dry in other seasons. Seasonal inundation represents the episodic events such as flooding and rising rivers. Permanent water is present in river channels and lakes that have water all year. Nonwater is in an anhydrous state all year.

There are four seasons in northeastern China, which can be merged into two seasons according to whether there is snow or ice cover. The snow season extends from November to May, and the rain season is from June to October. The water types are then defined based on the



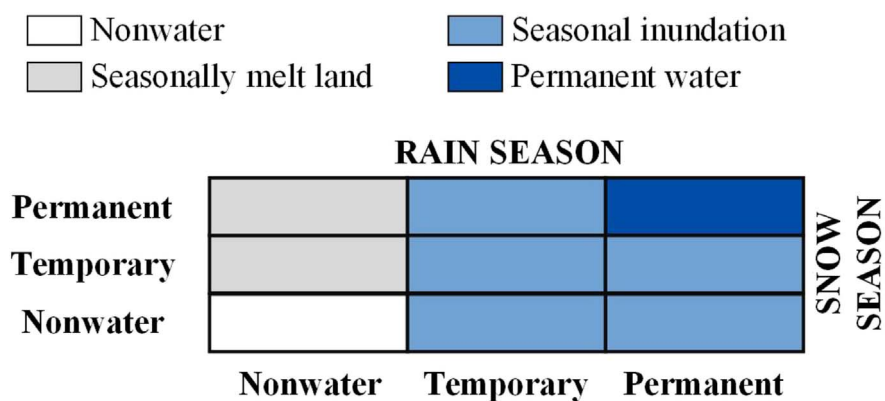


Fig. 6. Four water subtypes regrouped from three types in seasons. The snow season is from November to May, and the rain season is from June to October.

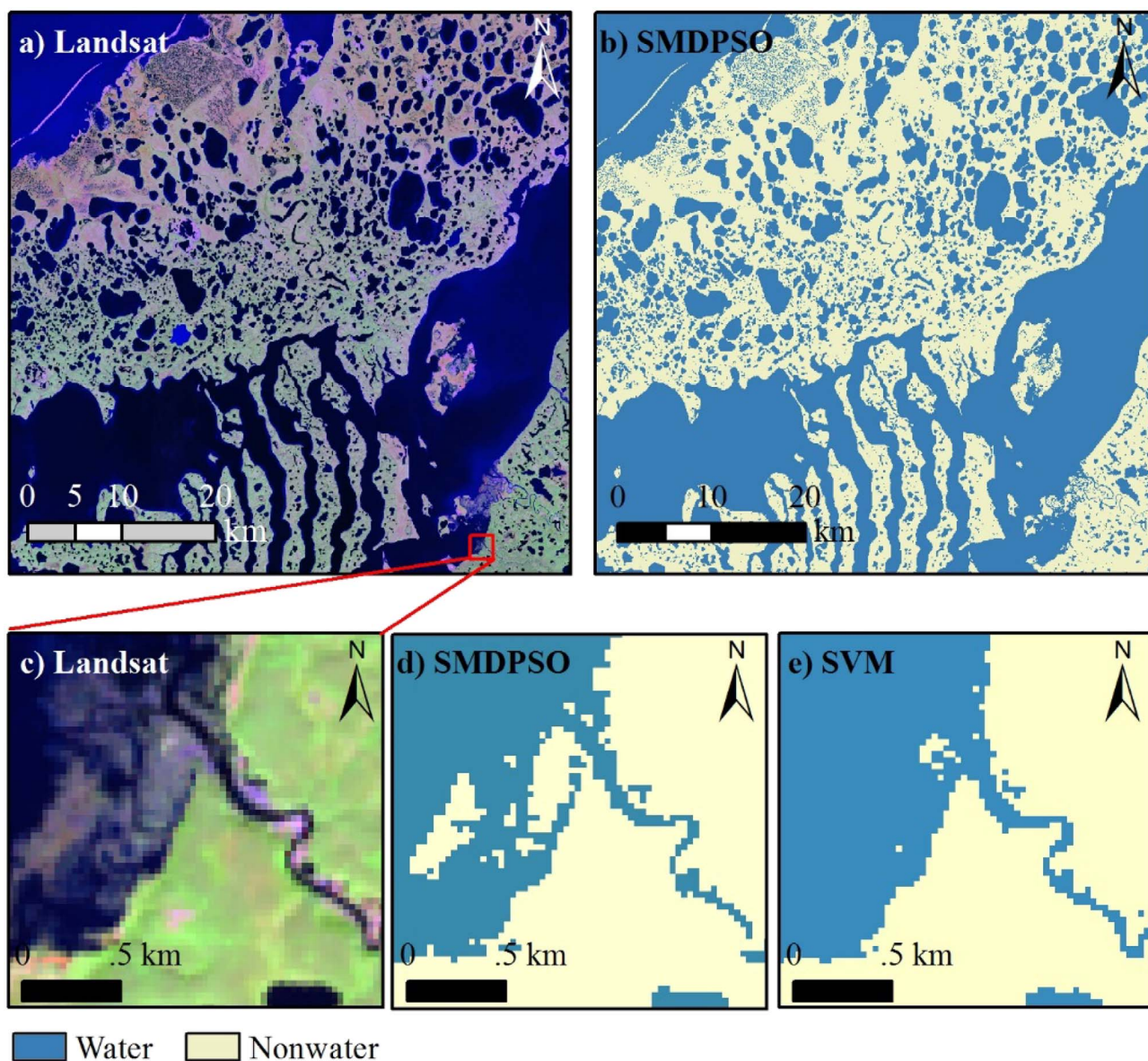
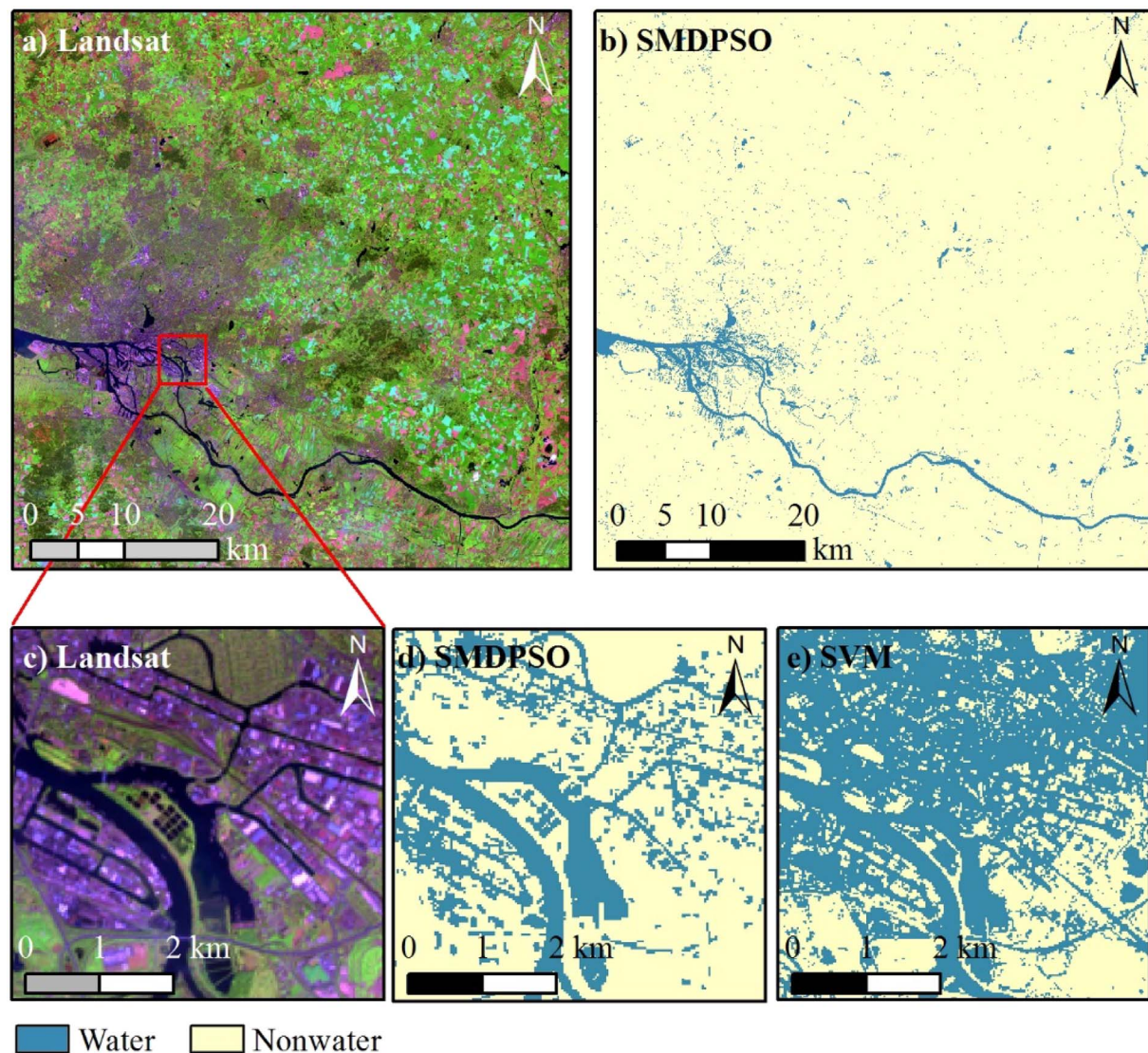


Fig. 7. SMDPSO performs better for shallows in Lake Tuktoyaktuk Canada (site A). a) Landsat 8 multispectral images in false color composite of SWIR 1, NIR and green bands, acquired 09/Jul/2013. b) SMDPSO classification. c) Landsat 8 multispectral images as a subset of a). d) SMDPSO classification as a subset of b). e) SVM classification as a subset of a). (For interpretation of the references to color in this figure legend, the reader is referred to the web version of this article.)





**Fig. 8.** SMDPSO correctly shows the real distribution of urban water in Hamburg (site C), with less influence of water-mixed pixels and dark vegetation. a) Landsat 8 multispectral image in false color composite of SWIR 1, NIR and green bands, acquired 12/May/2016. b) SMDPSO classification. c) Landsat 8 multispectral image as a subset of a). d) SMDPSO classification as a subset of b). e) SVM classification as a subset of a). (For interpretation of the references to color in this figure legend, the reader is referred to the web version of this article.)

inundation frequency in each season. For example, nonwater indicates pixels with an inundation frequency of < 1%, temporary water applies to pixels with an inundation frequency between 1 and 90% and permanent water regions have an inundation frequency > 90%. The four subtypes are defined by a combination of three types. Seasonal melt land is pixels that are nonwater pixels in the rain season and permanent or temporary water in the snow season. Seasonal inundation has five combinations: permanent in the rain season and temporary/nonwater in the snow season; and temporary in the rain season and permanent/temporary/nonwater in the snow season. Permanent water is pixels that are permanent water pixels in both seasons. Nonwater is applies to pixels that are nonwater pixels in both seasons. The combinations are shown in Fig. 6.

#### 4. Results

The SMDPSO classification results were compared with those of IsoData, K-Means, ML, NNC and SVM to visually and quantitatively assess the accuracy. The OA, KC, CE and OE were used as the evaluation indices. To demonstrate the regional universality of this method, all indices were computed for all eight test sites globally. Finally, a case of

flooding in northeastern China was evaluated to test the application of SMDPSO to map flood inundation.

##### 4.1. Accuracy and sensitivity assessment

Accuracy assessment and sensitivity analysis were used to evaluate the system. Accuracy assessment was implemented by visual and quantitative comparison. The sensitivity analysis investigated the influence of the water spectrum, tile size and specific features.

###### 4.1.1. Visual assessment

Water classification mapping for eight test sites was performed by SMDPSO with two classes: water and nonwater. The advantages of this method and its ability to identify specific features were demonstrated.

SMDPSO can precisely identify small puddles and thermokarst lakes in Tuktoyaktuk, Canada (Fig. 7). However, shallows have a spectrum similar to that of water and can easily be misclassified. As shown in Fig. 7, SVM recognizes much more water because of the misclassification of shallows as water. However, SMDPSO performs better by successfully removing more shallows.

Hamburg is an example of an aquatic city that is famous for its large



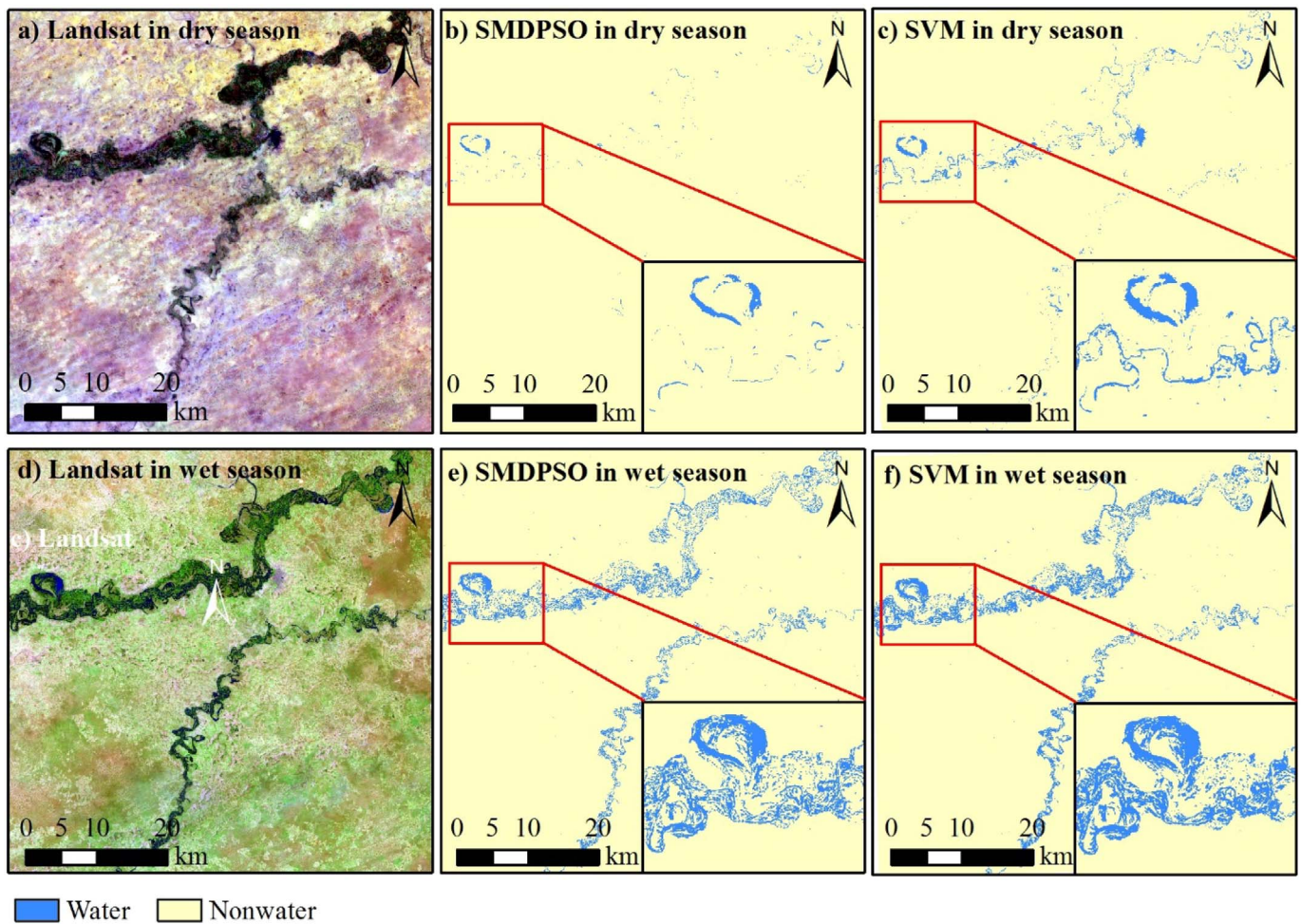


**Fig. 9.** SMDPSO performs better in the wet season than in the dry season for the Yobe River (Site D1 & D2). a) Landsat 8 OLI multispectral image in the dry season with false color composite of SWIR 1, NIR and green bands, acquired 23/Feb/2016. b) SMDPSO classification in the dry season. c) SVM classification in the dry season. d) Landsat 8 OLI multispectral image in the wet season with false color composite of SWIR 1, NIR and green bands, acquired 18/Sep/2016. e) SMDPSO classification in the wet season. f) SVM classification in the wet season. (For interpretation of the references to color in this figure legend, the reader is referred to the web version of this article.)

water bodies embedded in artificial surfaces (Fig. 8). These features lead to more errors of misclassifying nonwater as water. As shown in Fig. 8e, SVM classifies many nonwater pixels, such as impervious surfaces and dark vegetation, as water and thus loses the real distribution of water. SMDPSO can correctly distinguish water from water-mixed surfaces and is not influenced by dark vegetation (Fig. 8d).

The Yobe River, located in a tropical savanna climate, has distinct dry and wet seasons (Fig. 9). The valley dries out in the dry season, and the remaining small amounts of water and low shrubs reflect dark in Landsat images (Fig. 9a). By contrast, the river channel is filled with water in the wet season (Fig. 9d). SMDPSO can distinguish water from dark, dense vegetation in the valley in the wet season, but does not perform well in the dry season when the spectrum of water in the channels is similar to those of some dark surfaces, such as low shrubs.

A number of ponds, located in Kaifeng, are separated by upheaved bare land and mixed with the neighboring water in the ponds (Fig. 10). Consequently, the spatial distribution of the ponds may be lost and displaced by a larger puddle in remote sensing classification, as in the performance of SVM (Fig. 10e). SMDPSO classifies water based on the water spectrum, with which it is possible to distinguish the water of ponds from adjacent upheaved bare land. Fig. 10 shows that SMDPSO can extract ponds with clear edges and represent the real spatial structure of these small ponds.

For the other test sites, SMDPSO classification results with excellent performance are shown in Fig. 11. Water across tropical rainforests is

recognized well near Manaus (Fig. 11a). As shown in Fig. 11d, the river channels of a peninsula are clearly reflected, with the exclusion of dark pixels, such as dense vegetation, bare ground, and some small vegetated areas surrounded by broad water bodies. The Bay of Bengal is another humid site, characterized by interconnected waterways (Fig. 11i). Most of the channels in the river network are classified correctly, and only a few tributary endings are omitted or interrupted. SMDPSO also performs well in arid areas, such as the Coongie Lakes in Australia (Fig. 11e). Water bodies in salt lakes with low water levels are fully recognized whether they are entirely filled or partially dried up, as were the narrow passages connecting two neighboring lakes. In addition, salt speckles at the waterline are eliminated.

#### 4.1.2. Quantitative comparison with supervised and unsupervised classification

The SMDPSO assessment results were analyzed quantitatively through comparison with those of other classification methods, including two unsupervised classification methods (IsoData and K-Means) and three supervised classification methods (ML, NNC and SVM). The OA, KC, CE and OE of the different methods were compared.

SMDPSO performed best in terms of the OA and KC (Fig. 12). SMDPSO had the highest median OA (98.98%) and the lowest fluctuation (standard deviation of 0.79%). SVM performed well, although its median OA (98.72%) was slightly lower and fluctuated more (standard deviation of 7.26%) than that of SMDPSO. IsoData and K-



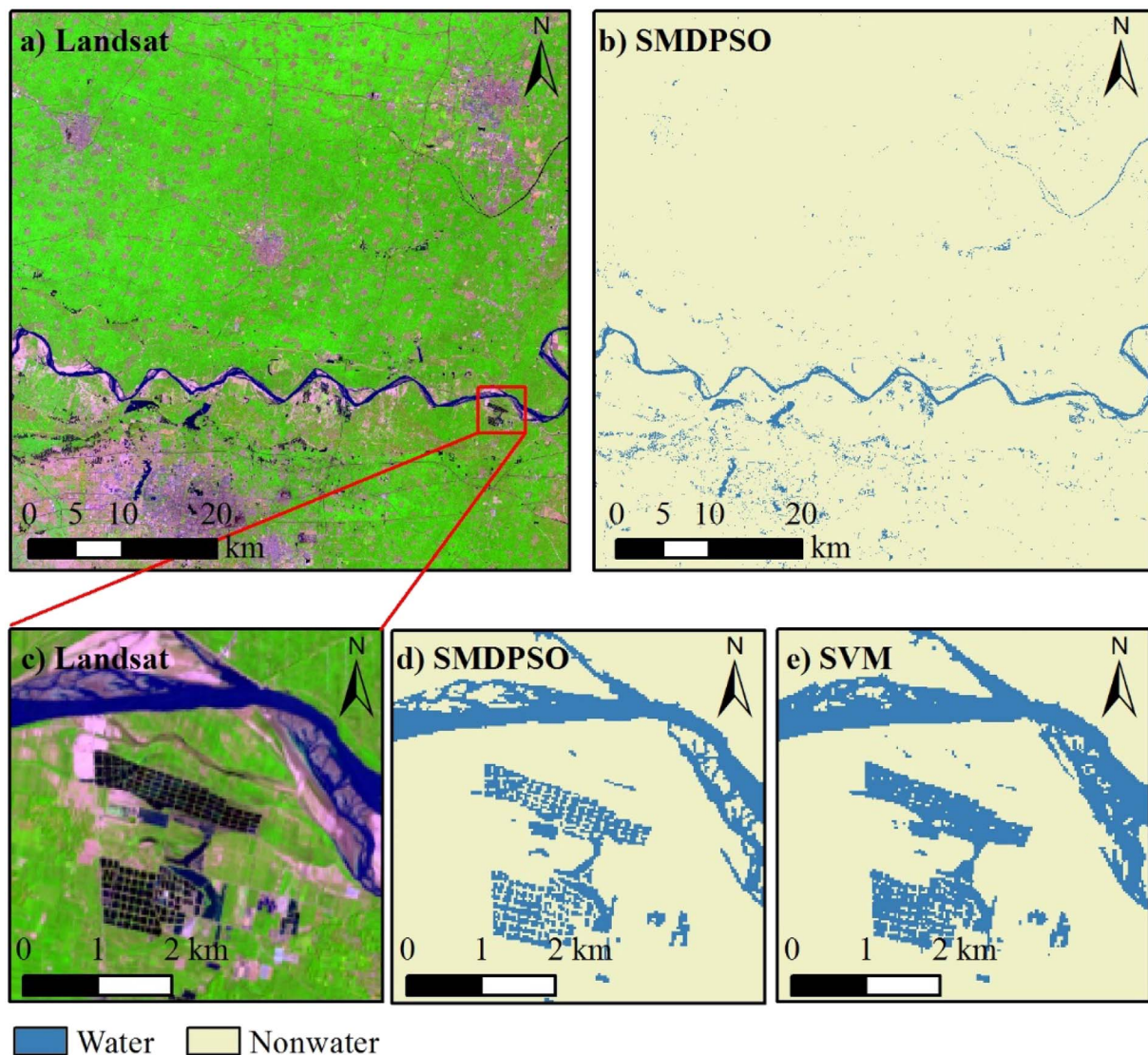


Fig. 10. SMDPSO can precisely extract small ponds with clear edges in Kaifeng (Site F). a) Landsat 8 multispectral image in false color composite of SWIR 1, NIR and green bands, acquired 04/May/2016. b) SMDPSO classification. c) Landsat 8 multispectral image as a subset of a). d) SMDPSO classification as a subset of b). e) SVM classification. (For interpretation of the references to color in this figure legend, the reader is referred to the web version of this article.)

Means fluctuated even more widely. In terms of OA, SMDPSO had the highest accuracy and was the most stable and therefore outperformed the unsupervised and supervised classification methods. Moreover, supervised classification was more accurate and more stable than unsupervised classification. SMDPSO also yielded the highest median KC (94.59%) with the least fluctuation (standard deviation of 15.06%). SVM and NNC showed greater fluctuation, although their values were lower than those of the unsupervised methods. In fact, the difference between SMDPSO and the other methods increased from OA to KC. Therefore, SMDPSO is more consistent with visually assessed images.

In terms of CE (Fig. 12), the median values for the supervised classification methods (ML: 0.02%, NNC: 2.65%, SVM: 3.71%) were much lower than those of the unsupervised classification methods (IsoData: 17.75, K-Means: 19.43%) and lower than that of SMDPSO (7.18%). However, the standard deviation of the CE of SMDPSO was the smallest. Therefore, SMDPSO misclassified nonwater as water more often than the supervised methods did but less often than the unsupervised methods did. However, the misclassification frequency of SMDPSO is more stable than those of the other methods Fig. 12.

For OE (Fig. 12), except for ML, all methods had the average OE values of < 10%. Additionally, except for ML, the methods showed

steady fluctuation. SVM and K-Means performed in terms of OE, although they also had abnormal values. The median OE of SMDPSO (0.695%) was lower than those of the supervised (ML: 33.65%, NNC: 2.75%, SVM: 1.31%) and unsupervised (IsoData: 7.27%, K-Means: 2.24%) methods. Therefore, SMDPSO has the lowest likelihood of misclassifying water as nonwater on average, although its performance was unstable for some sites.

#### 4.1.3. The sensitivity analysis to standard water spectrum

SMDPSO is less sensitive to the inland water spectrum, and can use only a portion of the water spectrum to obtain classification results. As shown in Fig. 13, the inland waters (i.e., Tanganyika, Taihu and Amur) were nearly equal with high OA, but the center of each point of Lake Tanganyika is slightly below those of Taihu and Amur; therefore, shallow water results in higher accuracy.

Seawater in the Pacific is associated with significantly lower accuracy. For example, in D2, the OA for inland water is > 99.3% but that for the Pacific is < 98.3%. F and G show the same significant differences. Therefore, seawater is not suitable for use as the standard water spectrum in SMDPSO.

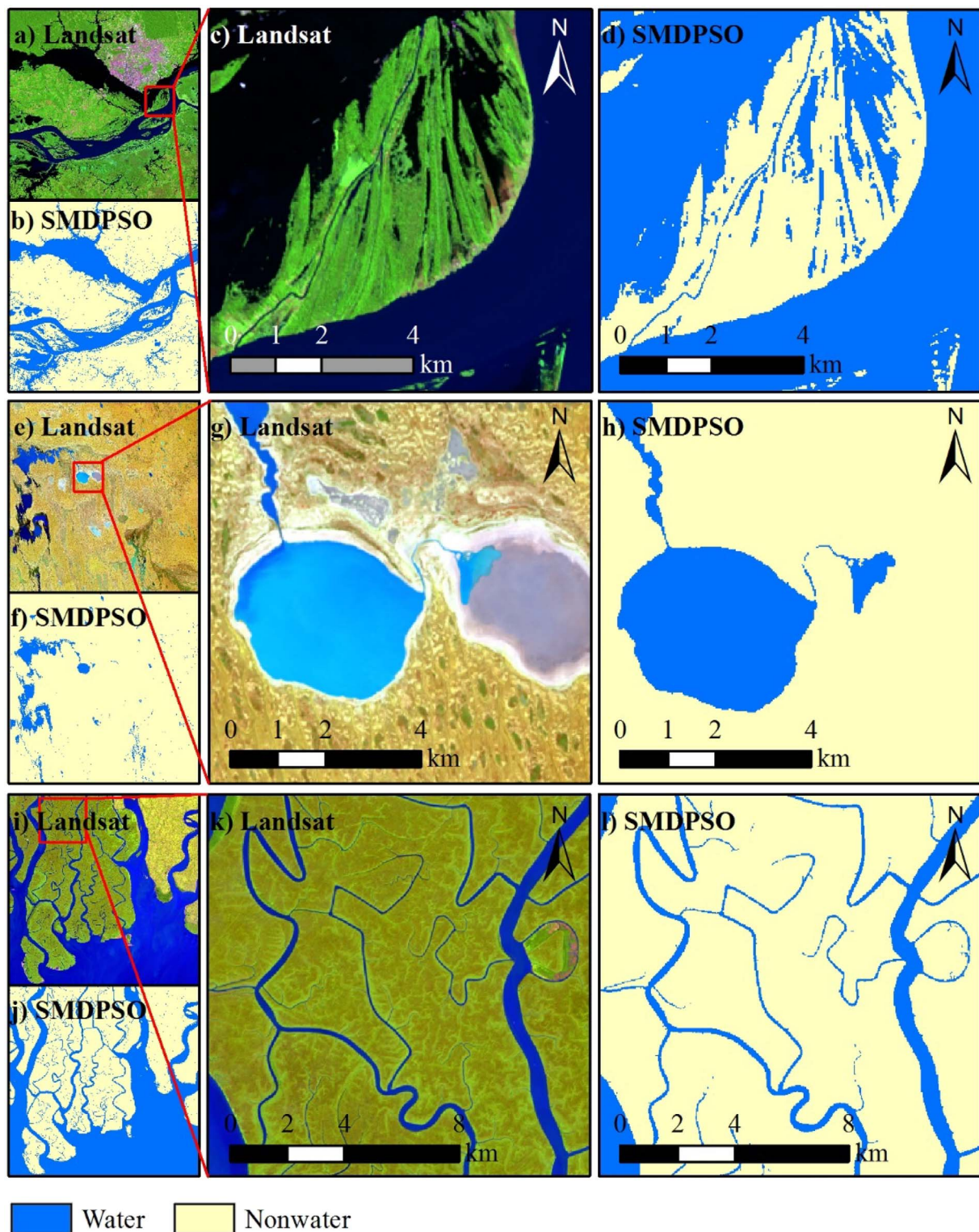


**Fig. 11.** SMDPSO performs well for Manaus (Site B, a–d), Coongie Lakes (Site G, e–h), and the Bay of Bengal (Site E, i–l). a) Landsat 8 multispectral image of Manaus, Brazil, in false color composite of SWIR 1, NIR and green bands, acquired 27/Jul/2016. b) SMDPSO classification in Manaus, Brazil. c) Landsat 8 multispectral image as a subset of a). d) SMDPSO classification as a subset of b). e) Landsat 8 multispectral image of Coongie Lakes, Australia, in false color composite of SWIR 1, NIR and green bands, acquired 06/Nov/2016. f) SMDPSO classification in Coongie Lakes, Australia. g) Landsat 8 multispectral image as a subset of e). h) SMDPSO classification as a subset of f). i) Landsat 8 multispectral image of the Bay of Bengal, in false color composite of SWIR 1, NIR and green bands, acquired 12/Nov/2015. j) SMDPSO classification in the Bay of Bengal. k) Landsat 8 multispectral image as a subset of i). l) SMDPSO classification as a subset of j). (For interpretation of the references to color in this figure legend, the reader is referred to the web version of this article.)

#### 4.1.4. The sensitivity analysis to tile size

To achieve the highest accuracy and satisfy the low time requirements, the best choice is a tile size of 4. As shown in Fig. 14, the maximum and minimum OA were achieved at a tile size of 4 and 12,

respectively, for all test sites. The OA of D1 was stable at values of 99.96–99.97%. However, the other seven sites showed apparent decreases in OA. As the size increased beyond 8, OA decreased significantly. Higher OAs (i.e., D1, D2, F and G), were more stable with



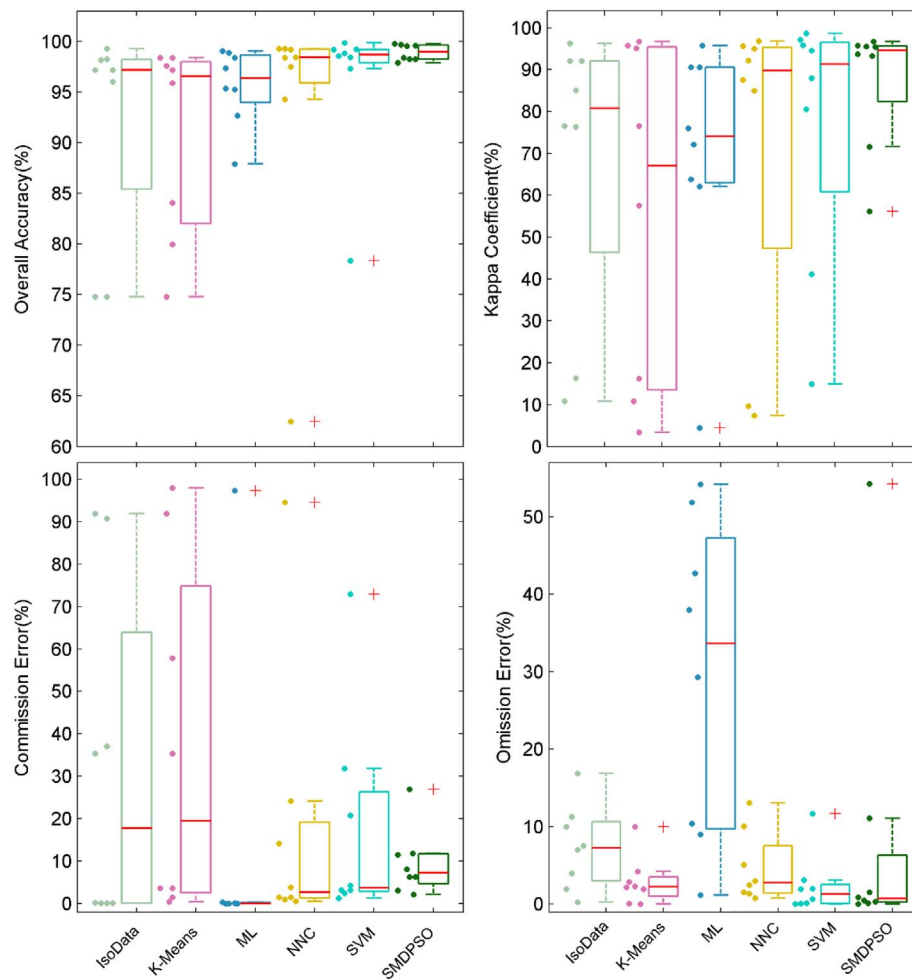


**Fig. 12.** Overall performance of SMDPSO compared with other methods, including IsoData, K-Means, ML, NNC and SVM. The dots distributed on the left of the boxes represent accuracy assessment values for the eight test sites in the corresponding method. The red line represents medians, and the red crosses indicate abnormal values. (For interpretation of the references to color in this figure legend, the reader is referred to the web version of this article.)

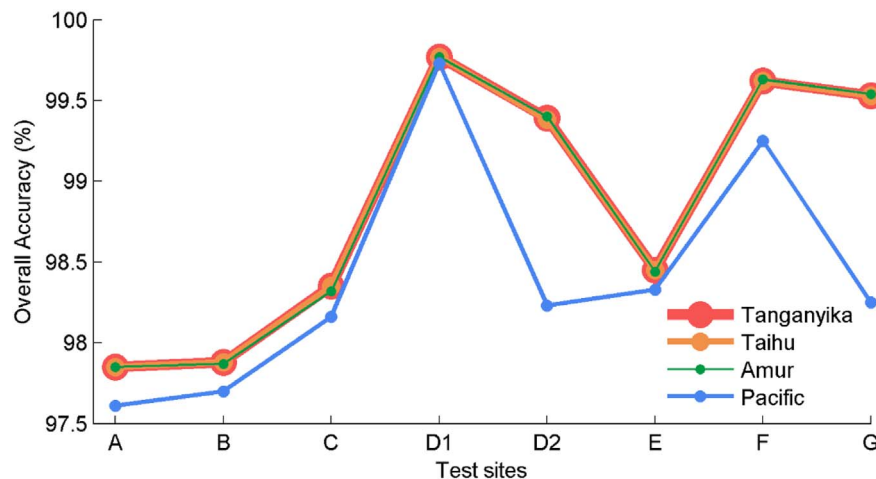


**Fig. 13.** Overall accuracy of water classification based on different standard water spectral curves. Tanganyika and Taihu are inland lakes, with deep and shallow water, respectively. Amur represents river water. The Pacific represents seawater, and shows significant difference from the other areas.

increasing tile size. Conversely, relatively low OAs (i.e., A, B, C and E) decreased faster.

#### 4.1.5. The sensitivity analysis to specific features

SMDPSO performs poorly for certain features because of the similarity of their spectra to the water spectrum. This poor performance is

observed in aquatic cities (e.g., wet wharfs), special buildings (e.g., airports) and inundation area between land and water.

The numerous canals that pass through Hamburg result in numerous water–urban mixed pixels (Fig. 15a), which are misclassified by SMDPSO as water. As shown in Fig. 15a, misclassification occurs when a wharf remains wet on the surface. Similarly, with the heavy summer



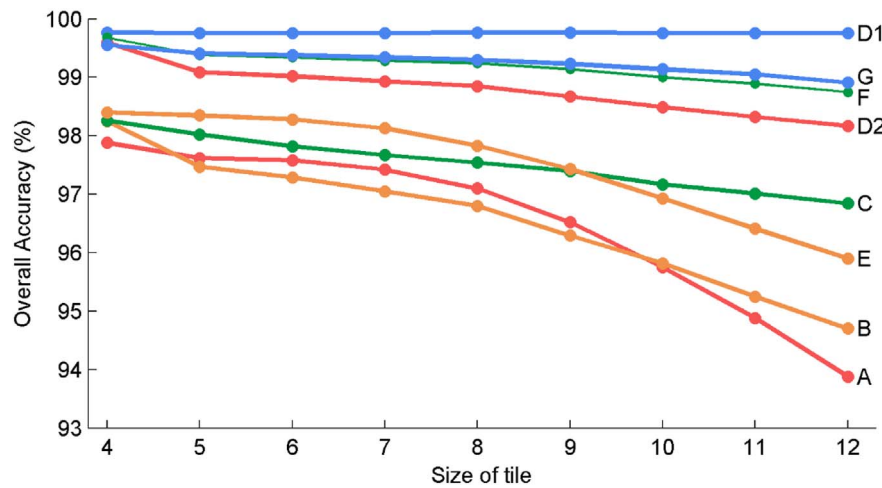


Fig. 14. Overall accuracy changes with increasing tile size for test sites A–G.

precipitation, the bare lands in dry areas of Australia are flooded, and shrubs near the lakeshore are inundated. In addition, the water spectrum is similar to that of these shrubs, which are shown as dark pixels in the satellite images. As a result, they are also identified as water (Fig. 15c).

Waterless artificial surfaces, such as narrow roads, bright white roofs and airports, are another source of interference. As shown in Fig. 15b, the runway and some buildings of the airport in Manaus were misclassified as water.

#### 4.2. A case of inundation mapping for flooding in northeastern China

SMDPSO can be applied to map flood inundation to better understand historical water distribution patterns and flood-affected areas. A flood in northeastern China in August 2013 is used as an example. The disaster area is very wet according to the inundation frequency (Fig. 16a). All the land in this area is covered by water with different frequencies. The southeastern and eastern parts are relatively dry. In addition to the permanent water (i.e., river channels, lakes and ponds), there is substantial seasonal melt land (Fig. 16b), which is covered in ice or snow in winter and is moistened as these features melt in spring. As shown in Fig. 16d, the surface land was still wet on June 1. Because of heavy flooding in 2013, much of the land was inundated (Fig. 16c), with a large seasonal inundation area. This region should be marked as a risk area for residents and requires greater attention for land use planning and disaster preparedness. This case demonstrates that SMDPSO is suitable for terrestrial water mapping as guidance for flood disaster management.

### 5. Discussion

This section addresses the low accuracy of some water classes. In addition, uncertainties, such as imperfections in SMDPSO, are noted and potential improvements are introduced.

#### 5.1. The low accuracy of some water classes

SMDPSO shows the highest accuracy and robustness in terms of OA and KC, but slightly lower stability in terms of CE and OE. SMDPSO cannot be applied if mixed pixels have too much or too little water. For example, Hamburg contains substantial mixing of water and infrastructure, which results in a high CE for SMDPSO due to misclassifying the infrastructure as water. The highest OE occurs for the Yobe River in the dry season, because SMDPSO cannot distinguish water from extremely arid land. So that is why we choose four metrics for accuracy assessment.

Furthermore, SMDPSO does not consider the continuity between adjacent tiles. Trickle and some other small water classes may be disconnected. To solve this problem, tiles can be replaced with moving windows such that each pixel will have more than one class result. The final result is determined based on the largest overall result. However, this method increases the time complexity.

#### 5.2. The interference of shadows, ice and clouds

Three steps are generally included in flood inundation mapping: (1) distinguishing water from nonwater via a water extraction method; (2) eliminating noise, such as shadows and clouds, using other data, such as DEMs; and (3) constructing a time series for the spatial distribution of water. This study is focused mainly on the first step. Time series construction is also considered without applying noise reduction. Consequently, certain errors that occur must be considered here.

Ice strongly influences water extraction. For example, the land area of Tuktoyaktuk is covered in ice during winter, and river channels are clearly observed (Fig. S1a). SMDPSO cannot differentiate these features and mistakenly classifies them as the same. Hill shadows on mountain slopes are observed as dark pixels (Fig. S1b), which decrease the reflectance of features to be similar to the spectral characteristics of water. Snow on a mountain top is also confused with water (Fig. S1c), even though it is a bright reflective surface. Hill shadows and snow are misclassified as water. Clouds are another significant source of noise in three cases. Case I: Clouds are thin, and partially or completely block the land surface (Fig. S1c). If they are sufficiently thin, the land surface may be recognized correctly by SMDPSO without interference. Case II: Clouds cast shadows onto the land surface and thus replace the real reflective information of the features (Fig. S1c). This type of shadow is denser and darker than hill shadows. As a result, these shadows are falsely recognized as water with high probability. Case III: Clouds are thick and sufficiently large that no land surface information is captured by the satellite images (Fig. S1d). These clouds are also classified as water. The water areas are accurate in case I but are exaggerated in cases II and III.

The water spectral curve is extremely similar to the spectrum of hill shadows and cloud shadows (Fig. S2), therefore, it may be impossible for SMDPSO to distinguish water from these two features on the basis of only spectral characteristics. Other data source must be used, such as DEMs to retrieve slope information to rule out steep hill shadows, and time series images (Mueller et al., 2016) to determine stable surface features and eliminate occasional cloud shadows. Alternatively, researchers have proposed cloud shadow screening algorithms (Zhu and Woodcock, 2012; Goodwin et al., 2013). Fortunately, the spectral curves of ice, snow, and thin and thick clouds contrast with the spectral

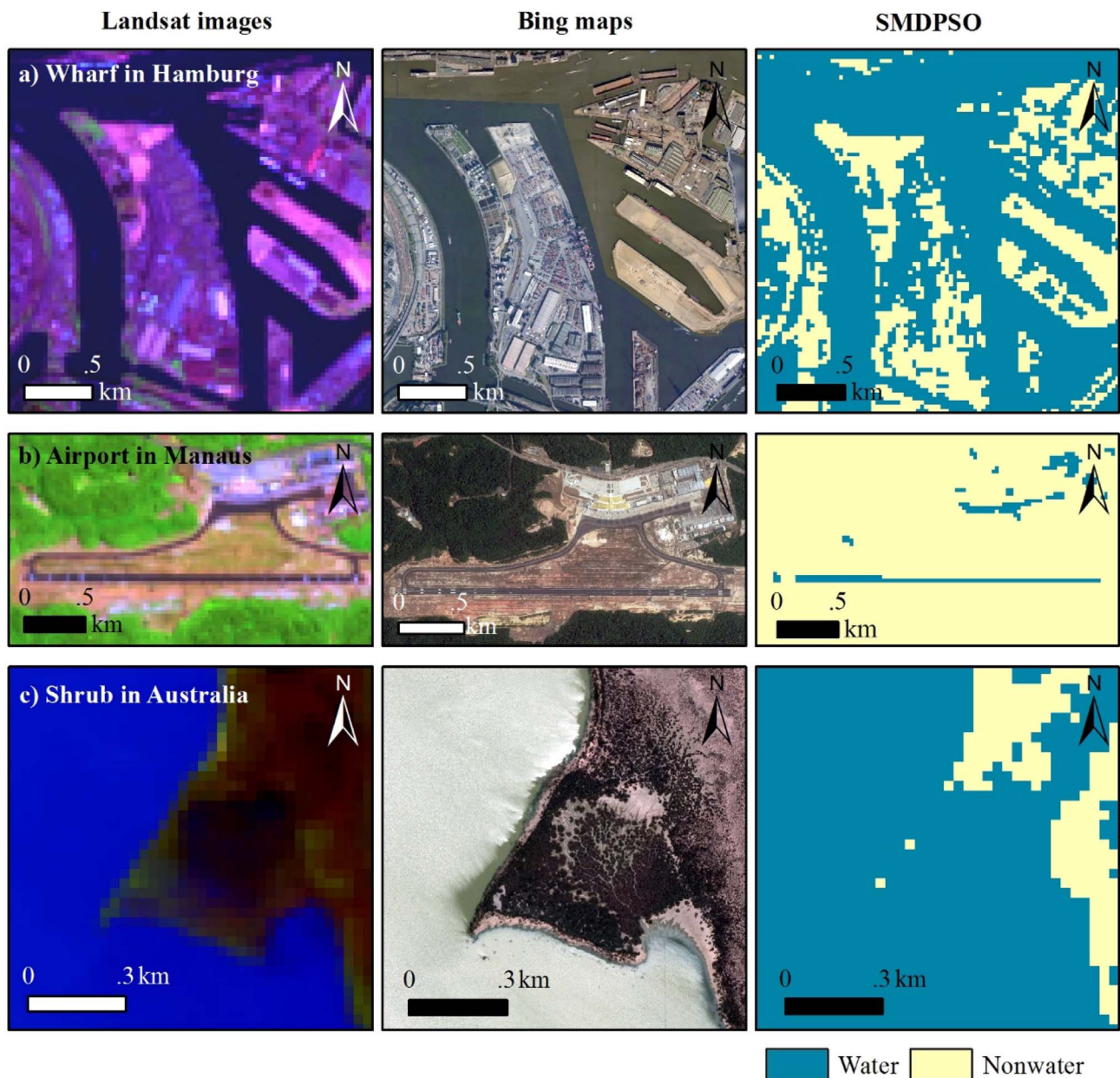


**Fig. 15.** Poor results of SMDPSO. The three columns show Landsat 8 multispectral images (RGB: SWIR 1, NIR, green), Bing maps satellites images (True Colors) and SMDPSO classification results, respectively. a) A wharf is misclassified as water in Hamburg (Site C). b) An airport is misclassified as water in Manaus (Site B). c) Shrubs near the lakeshore are misclassified as water in Australia (Site G). (For interpretation of the references to color in this figure legend, the reader is referred to the web version of this article.)

curve of water. SMDPSO considers only the differences between various bands and ignores the divergence of features in the same band. These features may be distinguished from water by considering the absolute spectral distance.

### 5.3. Further improvement

#### 5.3.1. Potential improvement for noise

Ice, snow and clouds are the main sources of noise that decrease accuracy, because SMDPSO highlights the relative differences in the spectral shapes and weakens the absolute distance between spectral curves. The spectra of these sources of noise, except shadows, are far from that of water (Fig. S2), and they can potentially be separated based on the relatively large spectral distance, despite their similar spectral shapes. One possible solution is to strengthen the spectral distance when calculating the distance similarity. However, it is impossible to distinguish shadows based on spectra. Other auxiliary data,

such as DEMs, are useful to correct the effects of shadows.

#### 5.3.2. Make full use of the normalized difference indices

Some normalized difference indices (NDI), such as NDWI, MNDWI, and AWEI, can be combined with spectral matching to provide greater discrimination. The water information will be enhanced and nonwater signals will be suppressed by integrating the spectral curve. According to Mueller et al. (2016), NDI<sub>52</sub> (NDI of band 5 and band 2), NDI<sub>72</sub> (NDI of band 7 and band 2) and NDI<sub>43</sub> (NDI band 4 and band 3) of Landsat TM are beneficial for water classification.

#### 5.3.3. Extend from Landsat OLI to other sensors

In this experiment, only Landsat 8 OLI images are considered, and the influences of different sensors, such as Landsat 5 TM, Landsat 7 ETM + and Sentinel-2, are ignored. Theoretically, SMDPSO is suitable as long as the input consists of multispectral images. However, two problems remain to be resolved. (1) Is the number of bands related to



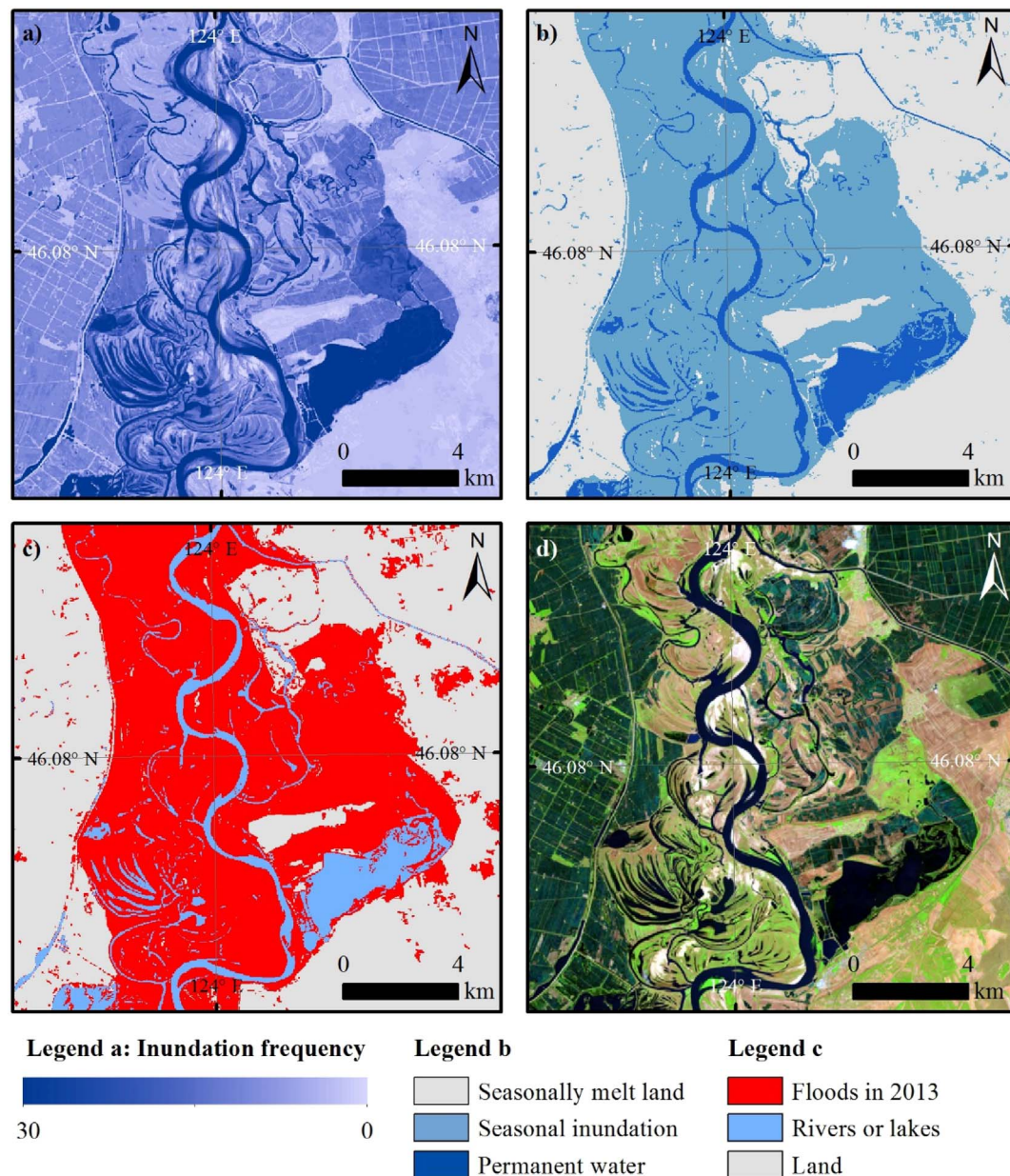


**Fig. 16.** A case study with SMDPSO for the northeastern China flood of 2013. a) Inundation frequency mapping from 2013 to 2016 using Landsat 8 OLI images. b) Water types identified from multi-year inundation frequency. Seasonal melt land is characterized by ice or snow that covers the land in winter and melts into water in spring. Seasonal inundation refers to temporary water that floods or dries out with seasonal changes. Permanent water refers to features such as long-term lakes, river channels, and puddle. c) Flood inundation mapping of northeastern China in 2013. d) Landsat 8 OLI images (RGB: SWIR 1, NIR, green) taken on June 1, 2013 before flooding.

accuracy, i.e., does including data from more bands yield more precise results? (2) How does the spatial resolution influence accuracy? For example, if Landsat 5 and Landsat 7 are suitable, all Landsat images with continuous time series (Wulder et al., 2016) over decades can be used to reconstruct water inundation frequencies from the 1980s to the present. Sentinel-2 has similar spectral and spatial characteristics as those of Landsat 8 (Storey et al., 2016), and their combined datasets provide more frequent temporal observations globally. Some previous studies (Zhu et al., 2015; Novelli et al., 2016) have been conducted with a combination of Landsat series and Sentinel-2 images. Therefore, the analysis of the sensitivity of SMDPSO to various sensors, especially similar sensors that have been used to construct long-term continuous data sets of observations with high and consistent spatial resolution, is important.

Reconstruct time series of water inundation. Water extraction is one step in surface water inundation mapping based on previous global or

continental surface water mapping (Yamazaki et al., 2015; Pekel et al., 2016; Sheng et al., 2016). Another important step is to reconstruct and analyze time series data. Various water types (e.g., permanent water, seasonal water and inundated areas) must be identified and noise, such as from cloud shadows cast on the surface, which are difficult to handle in the spatial domain, must be removed. Time series analysis in the time domain is an alternative method to reduce noise, but some important information, such data from extreme events (e.g., floods), is lost in the process.

## 6. Conclusion

The main purpose of this study was to propose a new water extraction method, named SMDPSO, with higher accuracy than that of supervised methods and less manual intervention than that of unsupervised methods and water index classification. Compared with



IsoData, K-Means, ML, NNC and SVM at eight global test sites, SMDPSO provided the highest accuracy and robustness. The input parameters, including the standard water spectrum and the tile size, are extremely stable; therefore, the values do not have to be changed for various situations. Thus, SMDPSO can automatically recognize water and non-water at different sites without manual intervention. According to these experiments, the suggested standard water spectrum for Landsat 8 OLI is {0.1153, 0.0942, 0.0779, 0.0715, 0.0324, 0.0055, 0.0031}, and the suggested tile size is 4. SMDPSO can successfully remove shallows and dark vegetation from water and preserve the real distribution of small ponds compared with unsupervised and supervised methods. Because of the spectral similarity, SMDPSO performs poorly for aquatic cities (e.g., wet wharfs), specific buildings (e.g., airports) and flooding area between land and water. Another problem with SMDPSO is that it fails to distinguish shadows, ice, snow and clouds without additional data. However, most of these sources of noise can be removed because their spectra differ from that of water.

The spectral matching method, a component of SMDPSO, is employed to compute the water probability. It fully utilizes all the bands, and thus mines more information than the previous water indices. A new water index can be developed based on the spectral characteristics of water, such as low reflectance and monotonicity. How to simplify the time complexity of SMDPSO while maintaining satisfactory accuracy is an important subject for future big data processing. Water extraction is only the first step in studying terrestrial water ecosystems. Our next objective is to provide a complete spatiotemporal framework for water inundation mapping with the application of time series analysis in the time domain.

## Acknowledgment

This work was supported by the National Key Research and Development Program of China (2016YFC0503002) and the National Natural Science Foundation of China (41571077 and 40701172). Appreciation goes to the editors and three anonymous reviewers for their valuable comments that have helped to improve this paper.

## Appendix A. Supplementary data

Supplementary data to this article can be found online at <https://doi.org/10.1016/j.rse.2018.02.012>.

## References

- Bazi, Y., Melgani, F., 2007. Semisupervised PSO-SVM regression for biophysical parameter estimation. *IEEE Trans. Geosci. Remote Sens.* 45 (6), 1887–1895.
- Bhatt, J.S., Joshi, M.V., Raval, M.S., 2014. A data-driven stochastic approach for unmixing hyperspectral imagery. *IEEE J. Sel. Top. Appl. Earth Obs. Remote Sens.* 7 (6), 1936–1946.
- Dudgeon, D., Arthington, A.H., Gessner, M.O., Kawabata, Z.-I., Knowler, D.J., Lévêque, C., Naiman, R.J., Prieur-Richard, A.-H., Soto, D., Stiassny, M.L.J., Sullivan, C.A., 2006. Freshwater biodiversity: importance, threats, status and conservation challenges. *Biol. Rev.* 81 (2), 163–182.
- Feyisa, G.L., Meilby, H., Fensholt, R., Proud, S.R., 2014. Automated water extraction index: a new technique for surface water mapping using Landsat imagery. *Remote Sens. Environ.* 140, 23–35.
- Goodwin, N.R., Collett, L.J., Denham, R.J., Flood, N., Tindall, D., 2013. Cloud and cloud shadow screening across Queensland, Australia: an automated method for Landsat TM/ETM + time series. *Remote Sens. Environ.* 134, 50–65.
- Kennedy, J., Eberhart, R., 1995. Particle swarm optimization. In: *Proceedings of IEEE International Conference on Neural Networks*, Pisataway, pp. 1942–1948.
- Li, L., Chen, Y., Xu, T., Liu, R., Shi, K., Huang, C., 2015a. Super-resolution mapping of wetland inundation from remote sensing imagery based on integration of back-propagation neural network and genetic algorithm. *Remote Sens. Environ.* 164, 142–154.
- Li, L., Chen, Y., Yu, X., Liu, R., Huang, C., 2015b. Sub-pixel flood inundation mapping from multispectral remotely sensed images based on discrete particle swarm optimization. *ISPRS J. Photogramm. Remote Sens.* 101, 10–21.
- Li, L., Xu, T., Chen, Y., 2016. Improved urban flooding mapping from remote sensing images using generalized regression neural network-based super-resolution algorithm. *Remote Sens.* 8 (8), 625.
- Marton, D., Kapelan, Z., 2014. Risk and reliability analysis of open reservoir water shortages using optimization. *Proc. Eng.* 89, 1478–1485.
- McFeeters, S.K., 1996. The use of the Normalized Difference Water Index (NDWI) in the delineation of open water features. *Int. J. Remote Sens.* 17 (7), 1425–1432.
- Mueller, N., Lewis, A., Roberts, D., Ring, S., Melrose, R., Sixsmith, J., Lymburner, L., McIntyre, P.A., Tan, P., Curnow, S., Ip, A., 2016. Water observations from space: mapping surface water from 25 years of Landsat imagery across Australia. *Remote Sens. Environ.* 174, 341–352.
- Novelli, A., Aguilar, M.A., Nemmaoui, A., Aguilar, F.J., Tarantino, E., 2016. Performance evaluation of object based greenhouse detection from Sentinel-2 MSI and Landsat 8 OLI data: a case study from Almería (Spain). *Int. J. Appl. Earth Obs. Geoinf.* 52, 403–411.
- Pekel, J.-F., Cottam, A., Gorelick, N., Belward, A.S., 2016. High-resolution mapping of global surface water and its long-term changes. *Nature* 540 (7633), 418–422.
- Raymond, P.A., Hartmann, J., Lauerwald, R., Sobek, S., McDonald, C., Hoover, M., Butman, D., Striegl, R., Mayorga, E., Humborg, C., Kortelainen, P., Durr, H., Meybeck, M., Ciais, P., Guth, P., 2013. Global carbon dioxide emissions from inland waters. *Nature* 503 (7476), 355–359.
- Rogers, A.S., Kearney, M.S., 2004. Reducing signature variability in unmixing coastal marsh Thematic Mapper scenes using spectral indices. *Int. J. Remote Sens.* 25 (12), 2317–2335.
- Ron, K., Foster, P., 1998. Glossary of terms. *Mach. Learn.* 30 (2/3), 271–274.
- Sheng, Y., Song, C., Wang, J., Lyons, E.A., Knox, B.R., Cox, J.S., Gao, F., 2016. Representative lake water extent mapping at continental scales using multi-temporal Landsat-8 imagery. *Remote Sens. Environ.* 185, 129–141.
- Shi, Y., Eberhart, R., 1998. A modified particle swarm optimizer. In: *Proceedings of IEEE International Conference on Evolutionary Computation*, Anchorage, pp. 69–73.
- Stendera, S., Adrian, R., Bonada, N., Cañedo-Argüelles, M., Huguén, B., Januschke, K., Pletterbauer, F., Hering, D., 2012. Drivers and stressors of freshwater biodiversity patterns across different ecosystems and scales: a review. *Hydrobiologia* 696 (1), 1–28.
- Storey, J., Roy, D.P., Masek, J., Gascon, F., Dwyer, J., Choate, M., 2016. A note on the temporary misregistration of Landsat-8 Operational Land Imager (OLI) and Sentinel-2 Multi Spectral Instrument (MSI) imagery. *Remote Sens. Environ.* 186, 121–122.
- Tang, Z., Li, Y., Gu, Y., Jiang, W., Xue, Y., Hu, Q., LaGrange, T., Bishop, A., Drahota, L., R., 2016. Assessing Nebraska playa wetland inundation status during 1985–2015 using Landsat data and Google Earth Engine. *Environ. Monit. Assess.* 188 (12), 654.
- Ten Brinke, W.B.M., Knoop, J., Muilwijk, H., Ligtoet, W., 2017. Social disruption by flooding, a European perspective. *Int. J. Disaster Risk Reduct.* 21, 312–322.
- Tulbure, M.G., Broich, M., Stehman, S.V., Kommareddy, A., 2016. Surface water extent dynamics from three decades of seasonally continuous Landsat time series at sub-continental scale in a semi-arid region. *Remote Sens. Environ.* 178, 142–157.
- USGS, 2017a. USGS Global Visualization Viewer. January 13. <http://glovis.usgs.gov/>.
- USGS, 2017b. Using the USGS Landsat 8 Product. June 22. <https://landsat.usgs.gov/using-usgs-landsat-8-product>.
- Wulder, M.A., White, J.C., Loveland, T.R., Woodcock, C.E., Belward, A.S., Cohen, W.B., Fosnight, E.A., Shaw, J., Masek, J.G., Roy, D.P., 2016. The global Landsat archive: status, consolidation, and direction. *Remote Sens. Environ.* 185, 271–283.
- Xu, H., 2006. Modification of normalised difference water index (NDWI) to enhance open water features in remotely sensed imagery. *Int. J. Remote Sens.* 27 (14), 3025–3033.
- Yamazaki, D., Trigg, M.A., Ikeshima, D., 2015. Development of a global ~90 m water body map using multi-temporal Landsat images. *Remote Sens. Environ.* 171, 337–351.
- Yang, H., Du, Q., Chen, G.S., 2012. Particle swarm optimization-based hyperspectral dimensionality reduction for urban land cover classification. *IEEE J. Sel. Top. Appl. Earth Obs. Remote Sens.* 5 (2), 544–554.
- Yang, Y., Liu, Y., Zhou, M., Zhang, S., Zhan, W., Sun, C., Duan, Y., 2015. Landsat 8 OLI image based terrestrial water extraction from heterogeneous backgrounds using a reflectance homogenization approach. *Remote Sens. Environ.* 171, 14–32.
- Zhang, Q., Gu, X., Shi, P., Singh, V.P., 2017. Impact of tropical cyclones on flood risk in southeastern China: spatial patterns, causes and implications. *Glob. Planet. Chang.* 150, 81–93.
- Zhu, Z., Woodcock, C.E., 2012. Object-based cloud and cloud shadow detection in Landsat imagery. *Remote Sens. Environ.* 118, 83–94.
- Zhu, Z., Wang, S., Woodcock, C.E., 2015. Improvement and expansion of the Fmask algorithm: cloud, cloud shadow, and snow detection for Landsats 4–7, 8, and sentinel 2 images. *Remote Sens. Environ.* 159, 269–277.